Regional CO_2 and CH_4 inversion system using WRF-Chem (v4.4)/DART (v9.8.0) and continuous high-precision observations over the Korean Peninsula

Doyoon Kwon[1], Bonhoon Koo[1], Jooyeop Lee[1], Jeongwon Kim[1], Jaehyung Ahn[1], Jinkyu Hong[1], Eri Saikawa[2], Alexander Avramov[2], Changsub Shim[3], Je-Woo Hong[3], Daegeun Shin[4], Shanlan Li[4], Sumin Kim[4], and Sangwon Joo[4]

[1]Department of Atmospheric Sciences, Yonsei University, Seoul, 03722, Republic of Korea
[2]Department of Environmental Sciences, Emory University, Atlanta, GA, 30319, USA
[3]Korea Environment Institute, Sejong, 30147, Republic of Korea
[4]National Institute of Meteorological Sciences, Jeju-do, 63568, Republic of Korea

Correspondence to: Jinkyu Hong (jhong@yonsei.ac.kr)

Abstract Quantifying greenhouse gas (GHG) emissions over complex terrain remains a significant challenge for conventional inversion systems due to the high sensitivity of tracer transport to surface heterogeneity. We develop a high-resolution dual-species greenhouse gas (GHG) top-down inversion framework by integrating the Weather Research and Forecasting model coupled with Chemistry (WRF-Chem v4.4) and the Data Assimilation Research Testbed (DART v9.8.0) in a cycling ensemble Kalman filter system. Built on community tools, the framework is designed to be portable and configurable, enabling application to other regions, resolutions, and observing-system configurations (e.g., expanded surface networks and additional data streams). This framework jointly assimilates near-surface CO_2 and CH_4 concentrations to produce dynamically consistent updates of emissions. By employing a unified Eulerian framework that simultaneously updates meteorology and 3-D tracer fields, the system preserves the physical consistency between transport and concentrations, effectively reducing transport bias over the complex landscapes of the Korean Peninsula. To improve the simulation of GHG turbulent dispersion in the atmospheric boundary layer over complex terrain, we incorporate surface heterogeneity parameterizations (roughness sublayer and canopy height) into the model physics in the inversion system. The system assimilates high-precision continuous *in situ* observations from three World Meteorological Organization/Global Atmosphere Watch (WMO/GAW) stations to constrain CO_2 and CH_4 emissions. Prior flux estimates include anthropogenic emissions (EDGAR v8.0), biogenic exchanges (the region-optimized VPRM), biomass burning (FINN v2.5 data), and oceanic CO_2 exchanges (SeaFlux data). A twin OSSE (Observation system simulation experiment) demonstrates that a denser observing network substantially enhances the detectability of regional emission signals and provides a robust pathway for significant uncertainty reduction. These results underscore the framework's infrastructure-readiness to serve as a practical design tool for future observing-network expansion and to support high-fidelity sub-national MMRV assessments. In a 2020 case study, the top-down estimates improve the agreement with ground observations, reducing root-mean-square errors by 30–60 % and reducing mean bias of 1-10 ppm (CO_2) and 30-60 ppb (CH_4) at the high-precision surface observation sites. Independent aircraft profiles provide external evaluation and indicate

residual CH_4 discrepancies consistent with background uncertainties. Posterior adjustments suggest reduced CO_2 emissions over the Seoul Metropolitan Area and parts of the western coastal region and increased CH_4 emissions over inland agricultural source regions relative to the priors, highlighting priorities for follow-on evaluation of inventory components. Our posterior CO_2 total is broadly consistent with ROK-BTR at the national scale, while posterior CH_4 totals show weaker agreement with available bottom-up estimates, consistent with the larger structural uncertainty in CH_4 source characterization and spatial allocation noted in previous studies. Overall, the framework provides a reproducible, scalable pathway toward multi-platform (satellite, aircraft, shipborne) integration for regional-to-national GHG assessment.

1 Introduction

Anthropogenic emissions of greenhouse gases (GHGs) originate predominantly from fossil fuel combustion, land-use change, agricultural practices, and waste management. These emissions are the principal drivers of contemporary climate change. Reliable and continuous monitoring of anthropogenic GHG emissions is essential for the development of effective climate mitigation strategies, compliance with international climate agreements, and the formulation of informed policy decisions (IPCC, 2021; Friedlingstein et al., 2025). Under the Paris Agreement, national inventories serve as the principal reporting mechanism, delineating Nationally Determined Contributions (NDCs) and facilitating periodic stocktakes (UNFCCC, 2015). These inventories are a standard method within the Measurement-Monitoring-Reporting-Verification (MMRV) framework and rely on bottom-up methodologies based on activity data and emission factors within a tiered framework established by the Intergovernmental Panel on Climate Change (IPCC) (Ogle et al., 2013). However, their accuracy is often limited by incomplete or outdated activity data, coarse spatio-temporal resolution, diffusive GHG emissions, and systemic delays in updating or reporting inventories (Rogelj et al., 2016; Pauw et al., 2018). Even nations with advanced inventories encounter challenges in capturing rapid emission changes, fine-scale spatial heterogeneity, and localized sources, which undermines the inventory credibility and comparability of inventories (Denison et al., 2019; Nisbet et al., 2019; WMO, 2025).

Top-down approaches, which are based on atmospheric inverse modeling or atmospheric data assimilation (DA), offer independent assessments of emissions by constraining surface fluxes through atmospheric concentration measurements (Enting, 2002; Gurney et al., 2002; Weiss and Prinn, 2011; Oda et al., 2019; Janssens-Maenhout et al., 2020; Elguindi et al., 2020; Mueller et al., 2021; Deng et al., 2022; WMO, 2025). These methodologies are increasingly incorporated into MMRV frameworks (WMO, 2022; 2025). By reconciling observed atmospheric concentrations with emission fluxes, top-down approaches can identify unreported or misrepresented emission sources, detect biases, and provide spatially explicit, policy-relevant emission information (Mueller et al., 2021; Janssens-Maenhout et al., 2020). Recent advancements in observational infrastructure, including dense atmospheric observation networks, satellite platforms, and airborne measurements, have enabled top-down systems to resolve emission patterns at urban and sub-national scales, thereby enhancing the fidelity and applicability of MMRV systems (Lauvaux et al., 2020; Byrne et al., 2023; Velasco et al., 2023).

Atmospheric inverse modeling frameworks for GHGs typically employ either Lagrangian or Eulerian methodologies. Lagrangian-based inversion frameworks track air parcels backward from receptor sites, offering computationally efficient source attribution (e.g., Henne et al., 2016; Pisso et al., 2019; Sijikumar et al., 2023; Brunner et al., 2025; Bukosa et al., 2025). However, they depend on external meteorological fields and background GHG concentrations, which limits their capability to accurately represent complex boundary-layer dynamics (Bréon et al., 2015; Lauvaux et al., 2016; Dekker et al., 2017; Super et al., 2017; Gaudet et al., 2021; Nalini et al., 2022; Bukosa et al., 2025). Conversely, Eulerian frameworks solve advection-diffusion equations directly on fixed spatial grids, allowing for a physically consistent coupling of meteorology and tracer transport, particularly when integrated with ensemble-based DA techniques such as the Ensemble Adjustment Kalman Filter (EAKF) (Anderson, 2001, 2003; Kang et al., 2012; Gaudet et al., 2021). Notable examples of operational Eulerian systems include the NOAA (National Oceanic and Atmospheric Administration) CarbonTracker (van der Velde et al., 2018) and ECMWF (European Centre for Medium-Range Weather Forecasts)'s CAMS (Copernicus Atmosphere Monitoring Service) global reanalysis (Agustí-Panareda et al., 2023); however, these systems typically operate at relatively coarse resolutions of about 1° which limits their effectiveness in capturing fine-scale emission heterogeneity in urban or mountainous regions (Gurney et al., 2002; Locatelli et al., 2013; Zhang et al., 2014; Feng et al., 2019; Gaudet et al., 2021).

These limitations motivate high-resolution Eulerian DA frameworks that can consistently represent mesoscale transport and boundary-layer mixing over heterogeneous surfaces and exploit expanding observing systems. The Weather Research and Forecasting model coupled with Chemistry (WRF-Chem) provides high-resolution, online coupling of meteorology and chemistry, while the Data Assimilation Research Testbed (DART) offers a robust ensemble-based DA platform for dynamically updating meteorological and chemical states resolution. Accordingly, the WRF-Chem coupled with the DART has been used in CO_2 concentration, regional meteorology and air quality studies (e.g., Mizzi et al., 2018; Ma et al., 2020; Zhang et al., 2021a). Previous studies have demonstrated the feasibility of coupling WRF-Chem with DART for CO_2 flux inversion using satellite XCO_2 retrievals in an ensemble Kalman filter framework (Zhang et al., 2021a; 2021b; Jin et al., 2025). While these studies establish feasibility, single-species (CO_2) estimation constrained by intermittent satellite sampling was attempted and the extent of independent flux evaluation (e.g., using independent in situ/aircraft constraints) and controlled robustness tests (e.g., OSSE-style experiments and systematic sensitivity tests to key uncertainty settings) remains relatively limited for robust flux-inversion assessment. Furthermore, applications to CO_2 and CH_4 regional inversions at kilometer-scale transport resolution remain limited particularly in complex-terrain environments where transport–flux aliasing and representativeness errors can be substantial. To our knowledge, a fully documented WRF-Chem/DART regional inversion framework that simultaneously targets CO_2 and CH_4 emissions and assimilates both in situ GHG observations and meteorological fields within a cycling dual-state configuration has not yet been documented in the literature. The present study fills this gap by providing a reproducible dual-species (CO_2/CH_4) state-augmentation system, including explicit configuration choices (uncertainties, localization/inflation, observation selection, boundary condition handling) and controlled OSSE demonstrations alongside real-data experiments.

Here we extend the WRF-Chem (v4.4) and DART (v9.8.0) framework to implement a 9-km dual-species inversion system that cycles meteorological DA while assimilating near-surface CO_2 and CH_4 observations, directly updating meteorology and 3-D tracer fields and estimating surface flux adjustments through ensemble cross-covariances. We further incorporate surface-heterogeneity-related physics and land information (e.g., roughness-sublayer and canopy-height adjustments) tailored to the Korean Peninsula, where complex topography, coastal circulations, clustered emissions, and monsoon seasonality pose challenges for conventional inventories and coarse-resolution inversions (e.g., Hong and Kim, 2011; Hong et al., 2019; Hong et al., 2020; Lee et al., 2021; Kim et al., 2024). To demonstrate framework performance beyond a single real-data case, we conduct a controlled OSSE (Observation system simulation experiment) with synthetic observations to assess flux-signal detectability and uncertainty reduction under increased network coverage, and we evaluate a 2020 real-data application using concentration-space diagnostics, flux uncertainty reduction, and intercomparisons with multiple emissions datasets. Together, these assessments demonstrate the utility of the framework for policy support and effective (sub)national MMRV applications.

2 Description of CO_2 and CH_4 inversion framework

2.1 Atmospheric modeling system

Our GHG inversion framework integrates a regional Eulerian atmospheric chemistry model with an ensemble-based data assimilation system. Specifically, this framework employs the Weather Research and Forecasting model coupled with Chemistry (WRF-Chem v4.4; Grell et al., 2005) and the Data Assimilation Research Testbed (DART v9.8.0) (Anderson et al., 2009) for sequential data assimilation. WRF-Chem solves the fully compressible, nonhydrostatic Eulerian equations on a fixed spatial grid, and simulates atmospheric dynamics, physical and chemical processes, and chemical transport within a unified framework.

In the inversion system, WRF-Chem generates ensemble forecasts by simulating meteorology with surface fluxes and atmospheric transport processes of GHGs. Given the long atmospheric lifetime of GHGs, they have been simulated as passive tracers in mesoscale models (Dekker et al., 2017; Super et al., 2017; Zhao et al., 2023). WRF-Chem includes the module to simulate passive tracer transport of GHGs since WRF-Chem v3.4 (Beck et al., 2012). In WRF-Chem, distinct variables represent background, anthropogenic, biomass-burning, oceanic (CO_2 only), and biogenic components of CO_2 and CH_4. The model simulates their fluxes, transport, and diffusion processes driven by the meteorological field to obtain a three-dimensional concentration field on an hourly basis. The total concentrations are represented as the sum of the component variables, facilitating comparison with observed concentrations. CO_2 and CH_4 are treated as a passive tracer for our regional application because the relative chemical lifetime of CH_4 against OH is on the order of years (about 9 years), whereas typical air-mass residence times across our regional domain are <1 day (Callewaert, 2024; Zhao et al. 2020). Therefore, the implied fractional

loss is negligible compared to transport and emission uncertainties. In addition, large-scale chemical aging and seasonality are already reflected in the prescribed initial and lateral boundary conditions.

Notably, for better simulations of GHG transport over complex terrain, we used the revised WRF-Chem by replacing the default WRF canopy height with high-resolution (1km) spaceborne lidar-retrieved canopy height data (GLAS/ICESat) for a better representation of surface characteristics (Lee and Hong, 2016). To simulate realistic transport and dispersion of GHG in the PBL, we further adapted roughness sublayer (RSL) parameterization of Lee et al. (2020), which incorporated the RSL function from the unified theory of Harman and Finnigan (2007, 2008) and Harman (2012), into the revised MM5 surface layer scheme (Jiménez et al., 2012) and Noah land surface model in WRF. Hereafter, we refer to this modified WRF-Chem v4.4 as the WRF-Chem GHG.

Our study area consists of a single model domain with 9-km horizontal spacing of 97 × 136 grid points and 51 terrain-following vertical levels stretching from the surface up to 50 hPa at the upper boundary (Fig. 1). The model employed specific physics parameterization schemes (Kim et al., 2024 and references therein), including the WSM-6 microphysics, RRTMG shortwave and longwave radiation schemes, the Yonsei University scale-aware PBL scheme, Kain-Fritsch cumulus scheme, and the Unified Noah Land Surface Model (LSM).

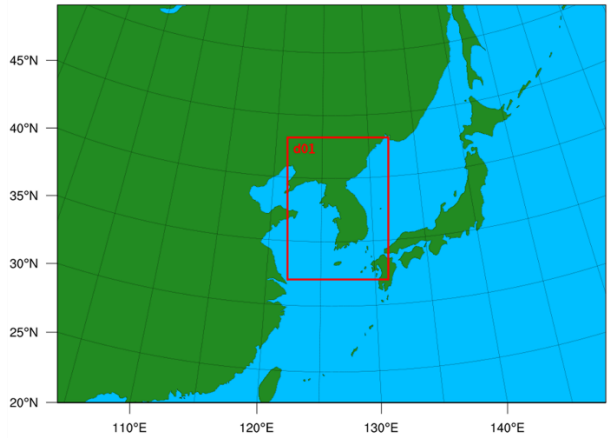

Figure 1. The WRF-Chem domain configuration used in this study.

2.2 DART data assimilation for GHG inversion

DART serves as a modular DA system designed to interface with various atmospheric models and observational datasets. The integration of WRF-Chem and DART enables the simultaneous assimilation of meteorological variables and chemical species through multivariate, dynamically consistent updates across the coupled system (Mizzi et al., 2016; Mizzi et al., 2018). The system operates as an ensemble of WRF-Chem forecasts, where each member represents a perturbed version of the state vector that accounts for both observational and model uncertainties. At each analysis cycle, ensemble perturbations are utilized to estimate a flow-dependent background error covariance, enabling the Ensemble Adjustment Kalman Filter (EAKF) to adjust

both meteorological and tracer fields simultaneously in a dynamically balanced manner. This ensemble-based structure allows for uncertainty propagation, sequential updating of the background (prior) ensemble, and the maintenance of consistency between state variables during sequential assimilation. Hereafter, we refer to the WRF-Chem GHG coupled with DART as the WRF-Chem/DART.

Our work extends the DA system to facilitate the simultaneous assimilation of observed CO_2 and CH_4 concentrations with meteorological data at a spatial resolution of 9 km over the Korean Peninsula. The assimilated data include continuous *in situ* CO_2 and CH_4 concentrations, alongside standard meteorological observations from National Centers for Environmental Prediction (NCEP) automated data processing upper air and surface observations (PREPBUFR observations). Because meteorology is simulated and updated within the online WRF-Chem/DART cycling system (rather than prescribed as offline transport fields), the inversion does not rely on externally prescribed meteorological trajectories and meteorological initial and boundary conditions (IC /BCs hereafter) are provided from standard large-scale reanalysis products as in limited-area modeling.

We use an ensemble size of 20 members throughout the cycling assimilations in the WRF-Chem/DART system. The analysis directly updates the prognostic meteorological variables and 3-D tracer concentration fields each cycle, while emission adjustments are estimated as surface forcing parameters for the subsequent forecast rather than being dynamically transported like tracer concentrations. This cycling approach helps preserve meteorology–transport–concentration consistency between the analyzed meteorology/tracer fields and the subsequent model transport in the ensemble forecasts. In the sequential EAKF framework, correcting the prognostic tracer concentration state at each analysis step helps prevent the carry-over of transport-driven concentration biases and reduces the risk that these biases are aliased into inferred emission adjustments. As demonstrated in previous WRF-Chem/DART studies (Liu et al., 2017; Hsu et al., 2024), failure to correct the concentration state allows transport-driven biases to persist into subsequent forecast steps. The filter would then continuously interpret these persistent concentration residuals as evidence of flux errors, leading to the artificial amplification of emission estimates (over-adjustment) to compensate for accumulated biases. By jointly updating the concentration state, the system effectively re-initializes the chemical conditions at each cycle, ensuring that emission adjustments are derived primarily from mismatches between model forecast and observation within the current assimilation window.

We implement this joint state–emission estimation using a state-augmentation approach in DART (Kang et al., 2011, 2012; Liu et al., 2017; Zhang et al., 2021a; Huang et al., 2022). The augmented state vector is defined as:

$$\boldsymbol{z} \equiv \boldsymbol{x} = \left[\boldsymbol{x}_{met}, \boldsymbol{x}_{chem}, \boldsymbol{x}_{flux}\right]^{\mathrm{T}} \quad (1)$$

where $\boldsymbol{x}_{met}$ contains meteorological variables including zonal and meridional wind, temperature, specific humidity, and surface pressure ($U,V,T,Q,$ and P_{sfc} respectively), $\boldsymbol{x}_{chem}$ contains three-dimensional CO_2 and CH_4 mixing ratios, and $\boldsymbol{x}_{flux}$ contains two-dimensional surface emission flux fields and is represented as time-indexed (e.g., hourly) flux fields that are

applied as external surface-forcing inputs to WRF-Chem during the subsequent forecast integration. At each analysis time, the deterministic EAKF updates the prior (background) augmented-state ensemble to the posterior ensemble:

$$\bar{z}^u = \mathbf{\Sigma}^u \left[(\mathbf{\Sigma}^p)^{-1} \bar{z}^p + \mathbf{H}^{\mathrm{T}} \mathbf{R}^{-1} \boldsymbol{y}^o \right] \tag{2}$$

$$\mathbf{\Sigma}^u = \left[(\mathbf{\Sigma}^p)^{-1} + \mathbf{H}^{\mathrm{T}} \mathbf{R}^{-1} \mathbf{H} \right]^{-1} \tag{3}$$

$$z_i^u = \mathbf{A}\left(z_i^p - \bar{z}^p \right) + \bar{z}^u, \qquad i = 1, \ldots, N \tag{4}$$

where $\bar{z}^u$ and $\bar{z}^p$ denote the posterior and prior ensemble means, respectively. The subscript i in z_i^p and z_i^u indicates the i-th member of the prior/posterior ensembles, and N is the ensemble size. $\boldsymbol{y}^o$ is observation vector including *in situ* CO_2/CH_4 and PREPBUFR meteorological observations, $\mathbf{R}$ is the observation-error covariance matrix, and $\mathbf{H}$ is the corresponding observation (forward) operator. $\mathbf{\Sigma}^p$ and $\mathbf{\Sigma}^u$ are the prior and posterior error covariance matrices, respectively. $\mathbf{A}$ is a transformation matrix satisfying $\mathbf{\Sigma}^u = \mathbf{A}\mathbf{\Sigma}^p\mathbf{A}^{\mathrm{T}}$ consistent with the EAKF adjustment used here. Equations (2) and (3) provide a compact summary of the linear Kalman analysis in information form. In practice, DART implements the Ensemble Adjustment Kalman Filter (EAKF) as a deterministic, serial ensemble update in observation space, where each observation is assimilated sequentially using ensemble-estimated covariances with covariance localization. The ensemble adjustment matrix $\mathbf{A}$ in Eq. (4) is computed so that the posterior ensemble anomalies reproduce the localized posterior covariance in Anderson (2001, 2003), thereby avoiding the sampling noise associated with stochastic perturbations of observations. We refer to Anderson (2001, 2003) and Anderson et al. (2009) for the detailed mathematical and theoretical backgrounds for EAKF.

For in situ CO_2 and CH_4, we specify the observation error variance as $\sigma^2 = \sigma^2_{\mathrm{meas}} + \sigma^2_{\mathrm{repr}}$, where σ^2_{meas} is the measurement uncertainty reported for the WMO/GAW stations (Lee et al., 2019; Lee et al., 2023) and σ_{repr} is treated as a model–data mismatch term, not as an instrument error, and its magnitude is chosen to maintain stable cycling behavior and to avoid overfitting sparse point observations in a 9-km grid framework. Because σ^2_{meas} is expected to be small for WMO/GAW-quality observations, σ_{repr} is treated as the primary contributor and is parameterized as a concentration-proportional term (as 5 % of the observed mole fraction) across all sites. This results in a relatively large effective error variance (typically ~20 ppm for ambient CO_2 and ~100 ppb of CH_4). This conservative parameterization is chosen not only to account for sub-grid variability but also to maintain analysis stability given the sparsity of the operational network. In data-sparse regions, relying too heavily on individual stations (via small observation errors) risks introducing spurious emission artifacts driven by local transport transients; a larger error specification mitigates this risk by ensuring that increments are driven only by persistent, robust signals. For PREPBUFR meteorological observations, we use the DART default observation error specifications.

Although the surface emission fluxes $\boldsymbol{x}_{flux}$ are not directly observed (i.e., **H** has no sensitivity to flux elements), they are updated through the ensemble cross-covariances $\mathrm{Cov}(\boldsymbol{x}_{chem}, \boldsymbol{x}_{flux})$. These flow-dependent covariances enable statistically consistent flux adjustments that reduce concentration innovations, provided that physically plausible concentration–flux relationships exist within the localization radius. As noted above, these flux adjustments are estimated as time-indexed forcing parameters rather than being propagated as a dynamic prognostic state. To suppress sampling error and spurious long-range correlations, we apply covariance localization using a Gaspari–Cohn polynomial with a horizontal half-width of 0.025 rad (~ 150 km) and a vertical normalization cutoff radius of 1.5 km, constraining increments primarily to the lower troposphere and reducing under-sampling error (Gaspari and Cohn, 1999; Anderson, 2012; Kang et al., 2012). Cross-species covariances are not applied; CO_2 and CH_4 tracers are updated independently. To mitigate ensemble under-dispersion, we apply adaptive prior inflation in DART (*inf_flavor* = 2). The inflation standard deviation is initialized at 0.6 and damped by a factor of 0.9, with the maximum allowed change per cycle limited to 1.05.

Prior uncertainty is represented by applying Gaussian, multiplicative perturbations to the chemical initial state, lateral boundary conditions, and anthropogenic emission fluxes when generating the forecast ensemble. For each ensemble member, perturbation factors are drawn from normal distributions centered at unity, with 1σ standard deviations of 5% for chemical initial and lateral boundary conditions and 30% for anthropogenic fluxes. The former represents a pragmatic balance between acknowledging residual uncertainty in the reanalysis inflow and preventing ensemble over-spreading that would overwhelm regional increments, while the latter is chosen to span the inter-inventory discrepancies over the Korean Peninsula (see Section 7.4 for details). The initial error configurations also align with those from previous studies (e.g. Zhang et al., 2021a, b). Horizontal and vertical correlation lengths are specified as 200 km and 1km, respectively.

Analyses are produced every six hours (00, 06, 12, 18 UTC) using observations within a ±3 h window centered on the analysis time; observations are rejected if they exceed three standard deviations of the background ensemble. The resulting analyzed ensemble is then advanced with WRF-Chem to provide the background for the next cycle, updating the chemical and meteorological initial conditions accordingly. To maintain dynamical consistency near the domain boundaries, the analysis increments are propagated consistently into the lateral boundary tendencies used for the subsequent forecast, preventing spurious discontinuities at the boundary interface. This is a numerical continuity treatment and does not constitute an independent optimization of boundary inflow.

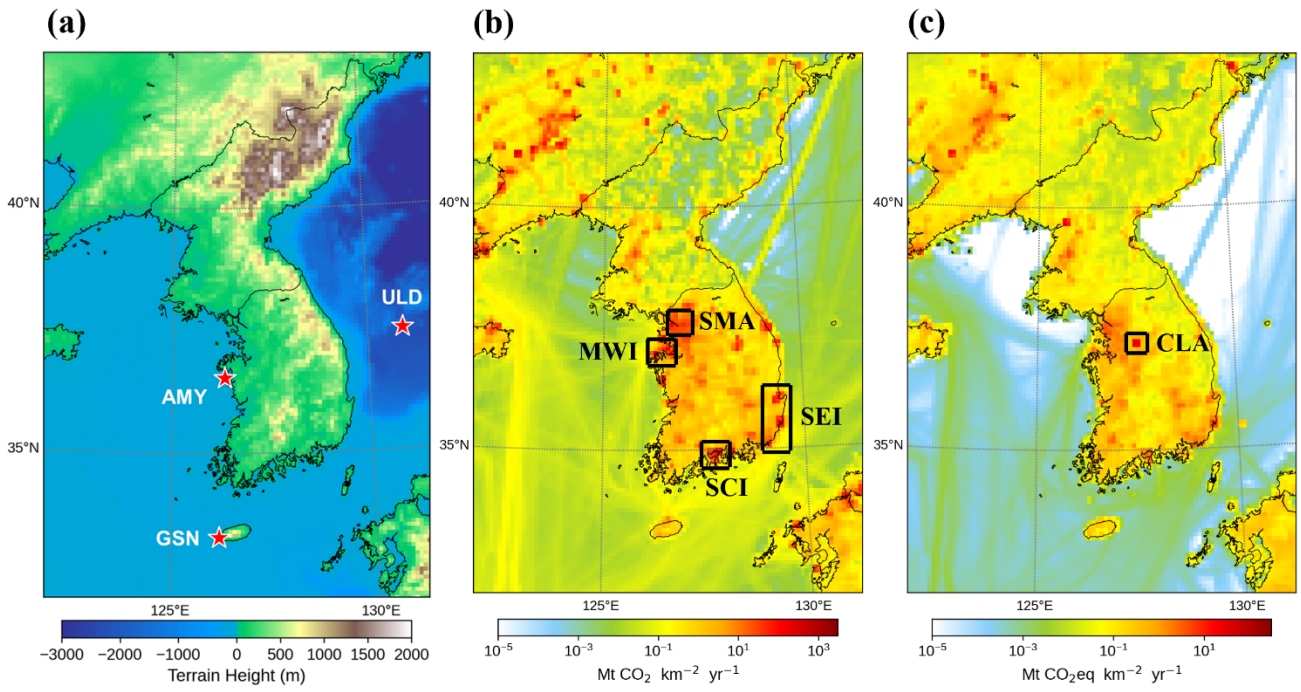

Figure 2. Locations of GHG monitoring stations (AMY, GSN, ULD) over terrain height (a) and annual anthropogenic emissions of CO_2 (b) and CH_4 (c) in the model domain in 2020 from EDGAR (v8.0). Main emission source regions in the model domain are boxed: (SMA: the Seoul Metropolitan Area, MWI: Mid-Western Industrial Area, SEI: SouthEastern Industrial Area, SCI: South Coast Industrial Area, CLA: Central Livestock Area).

3 Observation data of GHG concentrations and meteorological conditions for data assimilation

High-precision, continuous ground-based GHG measurements are essential for capturing high-frequency variability and providing constraints on regional enhancements near major source regions. To constrain CO_2 and CH_4 fields, the inversion framework assimilates *in situ* measurements of CO_2 and CH_4 concentrations from World Meteorological Organization (WMO) Global Atmosphere Watch (GAW) affiliated monitoring stations at Anmyeondo (AMY), Gosan, Jeju Island (GSN), and Ulleungdo (ULD) operated by the Korea Meteorological Administration (Fig. 2a). Depending on wind direction and atmospheric stability, they sample background inflow and downwind plumes from key emission source regions (Fig. 2b and 2c). We therefore retain pollution events (no background selection) and rely on the coupled transport + localization to attribute information primarily within the dynamically connected influence region. The new surface parameterizations adopted in this study improve wind simulations near the surface (e.g., Lee et al., 2015; Lee and Hong, 2016; Lim et al., 2019; Lee et al., 2020;

Kim et al., 2024; Lee et al., 2024; Jo et al., 2025; WMO, 2025). For reference, we provide concise verification of modeled 10-m winds with Korea Meteorological Administration (KMA) ASOS observations at GSN and ULD and refer to Supplement (Fig. S1–S2 and Table S1).

Each site employs a harmonized measurement system based on cavity ring-down spectroscopy (CRDS, Picarro Inc., USA), paired with a custom cryogenic drying system jointly developed by KMA and the Korea Research Institute of Standards and Science. This setup ensures high-precision CO_2 and CH_4 measurements with minimal water vapor interference, critical for ensuring data quality under Korea's seasonally variable meteorological conditions. Data are collected at 1-minute intervals, processed hourly into Level-2 quality-assured products. Here, Level-2 denotes QA/QC screening and calibration processing, distinct from 'background-selected' products that apply additional baseline selection. All stations are operated as GAW monitoring stations with documented QA/QC and are used here to constrain regional-scale enhancements rather than micro-scale local fluxes. It is worth noting that this Level-2 dataset excludes instrumental artifacts (e.g., calibration periods) but retains local and regional pollution events without applying background selection filters, ensuring that the high-concentration signals required for regional inversion are preserved. Further details on instrument calibration, QA/QC protocols, and traceability to international standards for CO_2 and CH_4 observations at WMO/GAW sites in Korea can be found in Lee et al. (2019) and Lee et al. (2023), respectively.

In addition, we assimilate conventional meteorological observations from the NCEP PREPBUFR datasets. These include surface pressure, near-surface air temperature, wind speed and direction, and specific humidity, as well as sea surface temperature and upper-air wind observations (including satellite-derived winds, radiosonde soundings, and aircraft reports of winds, temperature, and humidity). Assimilating these data effectively constrains the meteorological state (winds, temperature, and humidity), thereby improving transport fidelity in the coupled WRF-Chem/DART system, consistently with the previous applications (Mizzi et al., 2016; Mizzi et al., 2018; Pouyaei et al., 2023).

4 Initial and boundary conditions for meteorological variables and GHG concentrations

Meteorological initial and boundary conditions are obtained from the ERA5 global reanalysis hourly single-level and pressure-level data at 0.25° × 0.25° resolution (Hersbach et al., 2020; Hersbach et al., 2023a, 2023b). The initial and boundary conditions are preprocessed by WRF Preprocessing System (WPS) to the model grid and then perturbed by WRF Data Assimilation System (WRFDA) based on previous studies (Barker et al., 2012; Mizzi et al., 2016; Liu et al., 2017; Zhang et al., 2021b).

Initial and boundary conditions of CO_2 and CH_4 are provided by the ECMWF CAMS global greenhouse-gas reanalysis (EGG4 hereafter) data (Inness et al., 2019; Agustí-Panareda et al., 2023). EGG4 applies 4D-Var data assimilation of *in situ* networks and satellite retrievals within the ECMWF's Integrated Forecast System (IFS Cycle 47R1) and currently covers the period of 2003–2020. The dataset provides atmospheric mixing ratio of CO_2 and CH_4, along with meteorological and chemical variables on regular 0.75° × 0.75° grid on 25 pressure levels and 60 hybrid σ-pressure vertical levels at 3-hourly intervals.

EGG4 data as initial and lateral boundary conditions help to ensure that large-scale seasonal and regional variability and the growing season CO_2 drawdown is represented in the background fields.

Previous evaluations indicate that EGG4 reanalysis data may exhibit systematic biases. Overall errors in CO_2 and CH_4 concentrations are within 10 ppm and 40 ppb near the Earth's surface (Agustí-Panareda et al., 2023). Validation of EGG4 data against Total Carbon Column Observing Network (TCCON) measurement shows standard deviations of the difference of 1.18 ppm for XCO_2 and 11.3 ppb for XCH_4 (Wang et al., 2023). Notably, it has been reported that EGG4 data have positive bias of CO_2 concentration in high emission regions, and its mean bias is about 7.46 ppm in Asia (Custódio et al., 2022). Regional biases can be systematic and location-dependent; for example, a negative bias of about 30 ppb in CH_4 concentration has been reported at the NOAA flask site in the mid-western industrial region (MWI) (Segato et al., 2025). We also note that even though EGG4 accounts for large scale CH_4 oxidation, is uses prescribed OH fields (or climatological loss rates) rather than interactive chemistry. Consequently, this reliance on a parameterized sink can contribute to systematic errors in CH4 concentrations, particularly where the prescribed loss rates do not reproduce local and temporal variability of photochemical loss properly (e.g., Zhao et al., 2020; Agustí- Panareda et al., 2023). We summarize these boundary-driven bias characteristics as diagnostic context to motivate our boundary-condition uncertainty treatment and to aid interpretation of residual baseline behavior discussed in Section 7.

5 Prior fluxes

5.1 Anthropogenic emissions

Within the domain, WRF-Chem simulates GHG transport and adds contributions from local surface emissions and sinks. Anthropogenic CO_2 and CH_4 emissions used as prior fluxes are regridded from EDGAR global GHG emission inventory version 8.0 (Crippa et al., 2023). EDGAR provides anthropogenic emissions data in accordance with IPCC-compliant methodologies based on international activity data and emission factors (Janssens-Maenhout et al., 2019, Crippa et al., 2024). In EDGAR, the sectoral composition differs markedly between CO_2 and CH_4 over South Korea. CO_2 emissions are dominated by the power, energy, industrial sectors (combustion and processes), with additional contributions from transport, fuel exploitation, and buildings (and minor contributions from remaining sources). In contrast, CH_4 emissions are dominated by agriculture and waste, followed by fuel exploitation, while other sectors are comparatively minor. It is also worth noting that wetland-like CH_4 emissions from rice paddies are categorized under the anthropogenic agricultural sector in EDGAR and are therefore included in our prior emissions. The inventory data used in this study, EDGAR does not include natural wetland methane emissions and it is reported that annual CH_4 emission from natural wetlands in Korea is about 0.001 – 0.01 Tg CH_4 (Zhang et al., 2025). This is less than 0.5% of national total anthropogenic CH_4 emissions.

Annual spatial distributions of CO_2 and CH_4 emissions across the domain are shown in Fig. 2. To consider temporal variability in CO_2 emission by human activities and disaggregate to hourly emissions, we apply the monthly and diel scaling factor reported by the EDGAR and the gridded Temporal Improvements for Modelling Emissions by Scaling (TIMES) factors,

respectively. These account for building heating/cooling usage patterns, traffic volume fluctuations, sectoral contributions (residential, commercial, transportation emission), and weekday-weekend differences at 0.25° × 0.25° resolutions (Nassar et al., 2013). Over ocean grid cells, EDGAR emissions are near zero except along major shipping lanes (if included in the selected EDGAR sectors).

The spatial distribution of annual anthropogenic CO_2 and CH_4 emissions highlights main source regions within the model domain (Fig. 2b and 2c). Strong CO_2 emissions in the Seoul Metropolitan Area (SMA) reflect aggregated contributions from power plants, traffic and building emissions in urban area. Industrial processes and power generation dominate emissions in the MWI and south and southeastern coast industrial corridors (SCI and SEI) over the Korean Peninsula (Fig. S3). CH_4 sources are generally coincident with strong CO_2 emission regions due to waste management in highly populated area but exhibits more spatially confined peaks with hotspots over the high-density urban area (SMA) (wastewater and landfills), central livestock area (CLA) (enteric fermentation and manure management) (Fig. S4).

5.2 Biomass burning emissions

Biomass burning emissions of CO_2 and CH_4 are taken from the Fire Inventory from NCAR (FINN version 2.5). This dataset estimates biomass burning emissions using burned-area calculations, year-specific land cover and vegetation datasets, fuel loading and emission factors, and the use of multiple fire-detection satellites such as MODerate resolution Imaging Spectroradiometer (MODIS) and Visible Infrared Imaging Radiometer Suite (VIIRS) (Schroeder et al., 2014). FINN provides emissions at 1 km spatial resolution and daily temporal resolution (Wiedinmyer et al., 2011; Callewaert et al., 2022; Wiedinmyer et al., 2023). The NCAR (National Center for Atmospheric Research) fire-emission preprocessing tool is used to subset the inventory over the modeling domain, regrid it to the model grid, and temporally disaggregate it to hourly emissions for the WRF-Chem GHG simulations. Biomass burning emissions show strong spatial and seasonal variability in our domain (Fig. S5 for CO_2 and Fig. S6 for CH_4). Seasonal enhancements are primarily observed in spring (March–May), possibly related to agricultural residue burning and land-clearing practices. The total contribution of biomass burning emissions over the Korean Peninsula is negligible compared with anthropogenic emissions (< 0.1%) during the study period (2020).

5.3 Ocean CO_2 exchanges

Air-sea CO_2 exchange is obtained from the latest SeaFlux Ocean Carbon Dioxide Flux product (v2023.02) (Roobaert et al., 2018; Fay et al., 2021; Roobaert et al., 2019). This dataset combines five meteorological reanalysis data with six ocean surface CO_2 datasets, making a total of 30 combinations of the data products. These data provide monthly ocean CO_2 fluxes on a 1°×1° grid for 1990-2022. For this study, ensemble-mean monthly exchanges are used for oceanic CO_2 fluxes and prescribed as hourly fluxes (i.e., held constant throughout each month without sub-monthly or diurnal variability). Monthly distribution of oceanic CO_2 exchanges over East Asia shows that the Yellow Sea and nearby shelves exhibit seasonal reversals in oceanic

CO_2 fluxes (i.e., net uptake during winter and spring and a source in summer) (Fig. S7) (Gregor and Fay, 2021). In contrast, the deeper East Sea acts as a persistent CO_2 sink. Although these patterns reflect known contrasts between shallow shelves and deep basins, the oceanic flux magnitude in our domain configuration is small relative to dominant anthropogenic and terrestrial biogenic CO_2 sources and sink.

5.4 VPRM-based estimation of terrestrial ecosystem fluxes

Terrestrial ecosystem carbon fluxes are estimated with the Vegetation Photosynthesis and Respiration Model (VPRM) coupled with the WRF-Chem. (Ahmadov et al., 2007; Mahadevan et al., 2008). VPRM simulates net ecosystem exchange (NEE) of CO_2 using meteorological drivers and satellite-derived surface indices, specifically the Enhanced Vegetation Index (EVI) and Land Surface Water Index (LSWI) from MODIS Terra surface reflectance 8-Day 500m product (MOD09A1). During model integration, VPRM computes GPP and ecosystem respiration (RES) and derives NEE as RESP-NEE (negative NEE indicates net uptake in our sign convention) for eight land-cover categories using EVI, LSWI, 2 m air temperature, and photosynthetically active radiation (PAR) derived from downward shortwave radiation simulated by the WRF-Chem. Vegetation inputs (plant functional type, EVI, and LSWI) are derived from the 1-km SYNMAP global land cover data and MOD09A1 and are preprocessed using the VPRM preprocessor (Jung et al., 2006). VPRM-derived terrestrial CO_2 fluxes are sensitive to parameters linking EVI, LSWI, temperature, and radiation to GPP and RES (Hilton et al., 2013; Dayalu et al., 2018; Li et al., 2020). Because each vegetation type has distinct responses to environmental drivers, parameter calibration is critical to reduce NEE biases with plant function types (PFTs). In this study, we adopt a single parameter sets (λ: maximum light use efficiency, PAR_0: half-saturation value of PAR, α: temperature sensitivity of respiration, and β: basal respiration rate) applied uniformly across PFTs (vegetation categories) reported by Li et al. (2020) which has been validated for East Asian land-cover conditions to better capture seasonal and ecological variations across the Korean Peninsula.

Terrestrial biogenic CO_2 fluxes from the VPRM show strong seasonality driven by photosynthetic activity and temperature-dependent respiration (Fig. 3a). Croplands, deciduous and mixed forests dominate in the model domain and contribute most to net carbon uptake during the growing summer season. Savanna and shrubland play minor roles in total uptake due to their limited areal extent. Monthly NEE shows clear net carbon uptake (negative values) in summer growing season (May to September) with the strongest uptake (i.e., most negative NEE) in July when GPP exceeds RES with relatively larger uncertainties in biogenic CO_2 fluxes. The monthly mean diurnal cycles of GPP, RES, and NEE further highlights daytime GPP peaks in summer mainly driven by higher incoming shortwave radiation and by more gradual, temperature-driven RES with the seasonal march of the summer monsoon (Fig. S8) (Hong et al., 2011). For 2020, the integrated NEE over South Korea is −43 Mt CO_2 (5% of national anthropogenic GHG emissions) and broadly consistent with the national inventory estimate of the Land Use, Land Use Change and Forestry (LULUCF) sink (−39 Mt CO_2; Ministry of Environment, Republic of Korea, 2025), indicating that the VPRM biogenic fluxes reasonably represent the terrestrial carbon sink in this system.

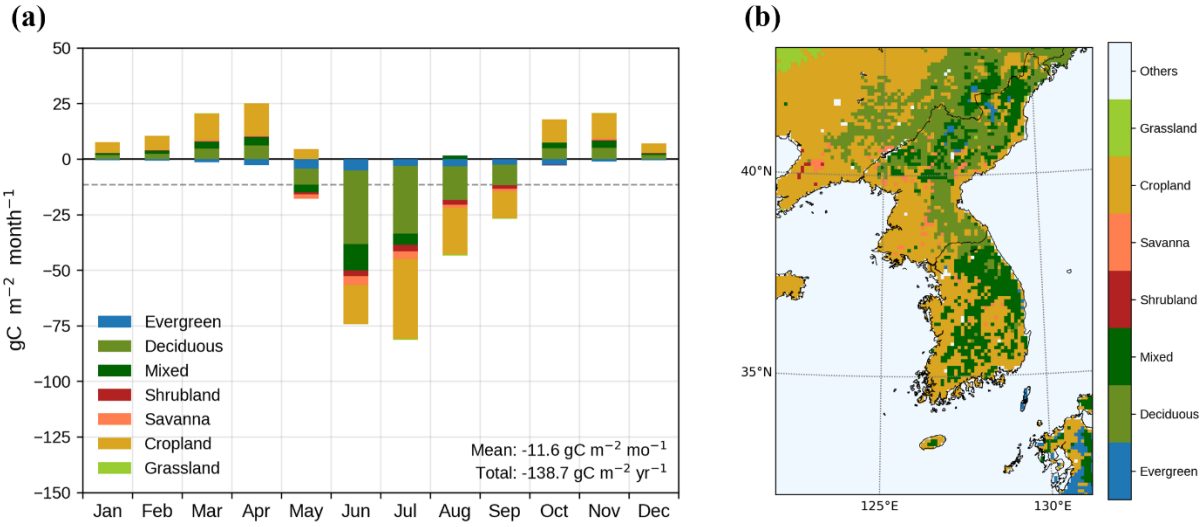

Figure 3. (a) Monthly net ecosystem exchange (NEE) contributions by vegetation class over the model domain in 2020. Bars show class totals (g C m^{-2} $month^{-1}$), computed as spatial averages over grid cells of the corresponding vegetation type; negative values indicate net carbon uptake. (b) Spatial distribution of dominant vegetation classes used in WRF-Chem/VPRM; each grid cell is assigned the class with the largest vegetation fraction. Colors are consistent across panels.

6 Observation system simulation experiment (OSSE) with an expanded surface network

6.1 OSSE overview and experimental objectives

To provide a self-consistent proof-of-concept of the coupled WRF-Chem/DART top-down GHG estimation framework, we conduct an Observation System Simulation Experiment (OSSE) that evaluates the system's flux recovery capabilities under a controlled, idealized experimental setup. The OSSE is designed as a standard twin experiment in which synthetic observations are generated from a "truth" simulation and subsequently assimilated to assess whether the system can recover the imposed emission signal. Here we focus on CO_2 to provide a compact and interpretable illustration of flux recoverability; the same assimilation architecture is directly applicable to CH_4; and both species are demonstrated in Section 7 using operationally available WMO-GAW *in situ* observations in a real-data application.

The twin experiment uses an expanded synthetic observing system comprising 50 surface sites, primarily concentrated over South Korea and located near major emission source regions. This hypothetical network is designed to test information gain under enhanced coverage, and to provide complementary evidence for how posterior constraints are expected to strengthen when observational coverage is substantially increased in a controlled twin setting. It is worth noting that this OSSE is a perfect-model twin experiment: the same WRF-Chem configuration (physics, meteorological IC/BCs, and model operators) is used for both the nature run and the assimilation experiments, and the only imposed difference is the anthropogenic emission field.

6.2 Controlled twin experiment with a synthetically imposed missing power industry emission signal

The OSSE is conducted for the 2020.03.01–2020.03.17 period. Data assimilation cycle iterates every 6 hours, starting at 00 UTC on 2020.03.03 and continues for 14 days, following a 48-hour spin-up. The nature run (representing the "truth") is generated with WRF-Chem using EDGAR CO_2 emissions for March 2020. This truth simulation is performed without data assimilation and provides dynamically consistent meteorology and tracer fields used to generate synthetic observations.

To define a clear and interpretable emission target for the OSSE, the corresponding inversion (prior) configuration uses EDGAR March 2020 CO_2 emissions with the power-industry sector removed ("EDGAR without power-industry"; Fig. 4a). This idealized "sector-removal" setup therefore benchmarks whether the assimilation system can recover the missing emission contribution (the "true difference") from concentration data under controlled, perfect-model conditions. The removed EDGAR power-industry sector accounts for 36.5% of domain-total CO_2 emissions, increasing to 44.7% of emissions over South Korea, thereby imposing a substantial signal for the assimilation system to recover. By removing such a major component, the experiment imposes a substantial, spatially localized signal that is, in principle, detectable. This ensures the OSSE presents a strong-signal recovery test rather than a weak-signal detection problem.

Synthetic observations are generated by sampling hourly nature-run CO_2 fields from 50 surface sites distributed across the model domain (shown as triangles in Fig. 4). The observation network in the OSSE is designed to cover strong CO_2 emission regions and maintain a minimum site spacing of approximately 30 km to increase sensitivity diversity while avoiding excessive redundancy in South Korea. Hourly CO_2 concentrations from lowest model level of the nature run are interpolated to each site location to construct the synthetic time series. The observations are assimilated using the same temporal handling as the cycling system (e.g., hourly observations assimilated within ±3 h window).

To emulate realistic measurement and representativeness uncertainty as in real applications, random observation error is introduced to each synthetic observation. These errors are assumed to be unbiased and Gaussian, specifically to match the real-data strategy described in Section 2.2: the error magnitude is dominated by the representativeness term and is parameterized as 5% of the sampled mole fraction. Ensemble perturbations for emissions and IC/BCs are generated following the exact strategy used in the real-data simulations. Furthermore, all other model inputs and ancillary datasets are kept identical to those in the real-data configuration to isolate the impact of observational density in a controlled twin setting.

6.3 Assimilation configuration for the OSSE

This OSSE is intentionally configured as a flux-recovery capability test under perfect transport*;* meteorological variables are excluded from the augmented state to isolate the concentration–flux mapping and avoid conflating flux recoverability with transport uncertainty. The real-data experiments retain the full dual-state configuration. The assimilation step in the OSSE follows the WRF-Chem/DART cycling framework described in Section 2: employing the EAKF with state augmentation to jointly estimate both GHG tracer field and surface flux parameter. The augmented state includes (i) 3-dimensional CO_2 mixing

ratios, and (ii) 2-dimensional anthropogenic flux scaling (or flux parameter) fields. The transport model configuration and meteorological IC/BCs are identical to those used in the synthetic truth generation.

Compared to the baseline real-data configuration, minor adjustments are made for the OSSE to ensure filter stability with the denser synthetic network. a minimum site spacing of approximately 30 km to increase sensitivity diversity while avoiding excessive redundancy. Specifically, the correlation length is set to 40 km and the localization half-width to 0.01 radians (~64 km) horizontally, deliberately avoiding over-tuning the system to the known truth. This configuration mimics a realistic operational capabilities assessment (where true error statistics are unknown) rather than a theoretically idealized scenario. This ensures that the evaluation isolates the impact of expanded network density, rather than the effects of perfect parameter optimization.

6.4 Emission estimation under a dense surface observational network

OSSE performance is evaluated against the known truth using diagnostics that target both emissions and concentration-space behavior. We examine: (1) the ability to recover the imposed emission signal (here, the missing power-industry contribution) via comparison of posterior emission increments with the known "true difference"; (2) posterior uncertainty reduction for emission parameters. The OSSE demonstrates that the assimilation effectively recovers the spatial structure of the imposed emission signal. The posterior emission increment (post–prior) exhibits a distribution that is broadly consistent with the "true difference" associated with the excluded power-industry emissions (compare Fig. 4b with Fig. 4a). The strongest adjustments occur in regions with the largest imposed emission differences and frequent downwind sampling by the expanded observing network. Correspondingly, posterior emission uncertainty reductions, quantified by the decrease in ensemble spread (standard deviation) relative to the prior, are concentrated and strongest near the synthetic site clusters and major source regions, yielding a domain-wide mean reduction of 18.1% and a larger reduction of 34.1% over South Korea due to the concentrated observation sites (Fig. 4c). The percent-change increment highlights where posterior adjustments are large relative to the prior magnitude (Fig. 4d), although this metric should be interpreted with caution in areas where prior emissions are very small.

In addition to the spatial diagnostics, we examine the South Korea–integrated CO_2 emission budget to quantify recovery of the imposed missing-sector signal in the best-observed region. We report both the mean flux correction integrated over the OSSE period and the equivalent annualized rate. Over South Korea, the gap between the truth ("control") and prior emissions is approximately ~215 Mt yr^{-1}. After the 14-day OSSE cycling period, the posterior emission closes 103.2 Mt yr^{-1} of this gap (a recovery rate of 49.3%). Expressed as an increment ratio, the assimilation increases total CO_2 emissions of South Korea by 21.5% relative to the prior. These recovery rates should be interpreted as a conservative lower bound. The partial quantitative recovery reflects two primary constraints: the short duration of the total assimilation period (14 days) relative to typical flux convergence timescales (monthly to annual), and the use of an operationally representative, conservative filter configuration (assuming observation errors of ~20 ppm). By avoiding idealized tuning—which would artificially maximize signal recovery in a perfect-model setting with substantially lower error characteristics—we demonstrate that the expanded network successfully identifies the spatial structure and direction of the missing signal even under a cautious data assimilation setup.

Thus, the results confirm robust signal detection capabilities, with the expectation that quantitative recovery would increase substantially over a longer period or with more optimized, situation-specific tuning.

Finally, it is important to note that the imposed power-industry signal is highly heterogeneous and dominated by discrete large point sources. Accordingly, the OSSE should be interpreted as a test of whether the system captures the dominant, observation-constrained emission corrections, rather than a pixel-by-pixel reconstruction of individual point sources. In addition, because emission updates are formulated with a prior-proportional (multiplicative) error structure, recoverability is inherently limited where prior emissions are near zero; this also motivates a cautious interpretation of percent-change increments in low-emission grid cells (Fig 4d). Overall, the OSSE constitutes a stringent stress test, and the coherent recovery of the main spatial signal and the localized uncertainty reduction near the dense observing network support that the framework is performing as intended.

6.5 Implications

The controlled twin-experiment provides a compact technical illustration of framework behavior under substantially expanded observational coverage. Using a dense 50-site synthetic surface network, the system produces coherent analysis increments and substantially stronger, more spatially informative emission constraints over the well-sampled region, reflected in larger posterior uncertainty reduction. Importantly, this behavior is demonstrated under an intentionally demanding target signal defined by omission of the power-industry sector, which is point-source-dominated and highly heterogeneous.

Crucially, these results were achieved using a standard, representative assimilation configuration rather than one hyper-tuned to the specific OSSE truth. The fact that the system successfully recovered the dominant spatial signals without requiring idealized, perfect-model parameter optimization underscores the robustness of the dense network itself. It suggests that the reported information gains are driven by the improved observational coverage, rather than by artificial tuning advantages.

These results additionally underscore the framework's powerful potential as a practical tool for designing and exploiting denser regional observing systems, with the goal of better diagnosing inventory uncertainties and supporting iterative inventory characterization and refinement. This OSSE clarifies the expected direction and spatial structure of constraint gains as observational density increases, providing a controlled complement to the real-data demonstrations that follow in the next section.

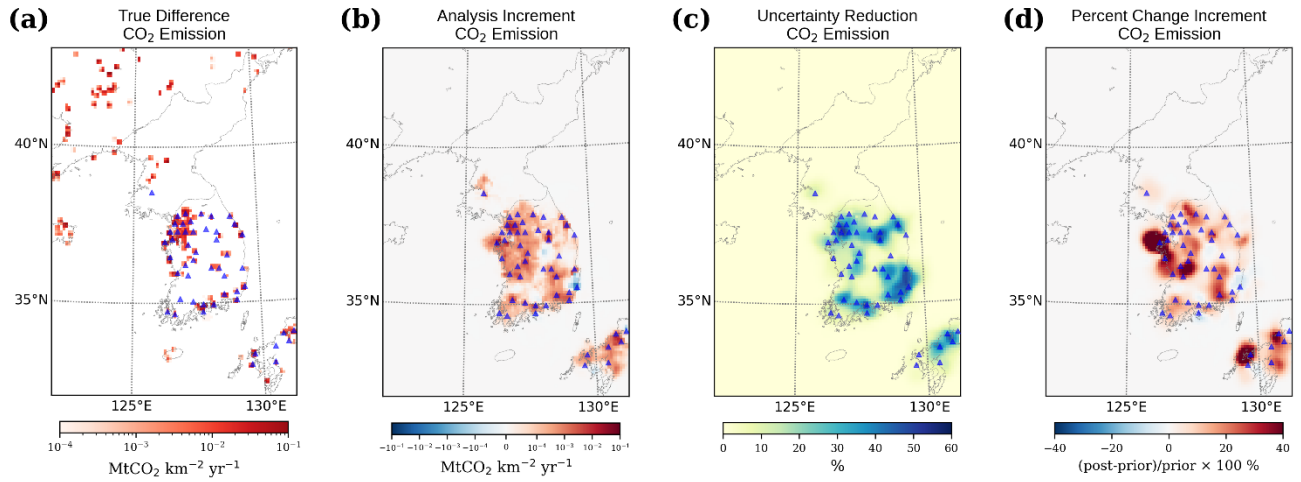

Figure 4. Temporal-mean OSSE diagnostics for CO_2 emissions using the expanded 50-site synthetic surface network over the OSSE DA cycling period (2020-03-03 00 UTC–2020-03-17 00 UTC). (a) Imposed target ("true difference" in CO_2 emissions), defined as EDGAR (full) minus EDGAR without the power-industry sector. (b) Analysis increment (posterior minus prior) in CO_2 emissions from the OSSE inversion. (c) Posterior uncertainty reduction for CO_2 emissions expressed as the percent decrease in ensemble spread (standard deviation) relative to the prior. (d) Percent-change increment in CO_2 emissions, computed as (posterior minus prior) divided by the prior. Triangles denote the locations of the 50 synthetic surface observation sites. All emission panels are shown in flux unit of Mt CO_2 km^{-2} yr^{-1}. Red (blue) shading indicates an increase (decrease) in the posterior relative to the prior. Panels (a) and (b) are displayed on a logarithmic color scale to visualize the highly skewed, point-source-dominated imposed signal, and percent-change increments in (d) are masked where prior emissions are below a small threshold to avoid spurious values.

7 Evaluation of the top-down estimates for 2020 case study

With the controlled proof-of-concept established in the previous section, we now present a real-data demonstration to assess how the same cycling and analysis configuration performs under real observational constraints and inevitable model-data inconsistencies. We evaluated inversion results for 2020 using the WRF-Chem/DART system with full DA, in which both meteorological and GHG observations were assimilated. Each monthly run was initiated at 00 UTC on the last day of the preceding month, followed by a 24-hour spin-up prior to the start of assimilation.

7.1 GHG concentrations at ground stations

Monthly distributions of prior, posterior, and observed CO_2 and CH_4 concentrations at the three WMO/GAW surface stations are summarized with box plots for comparison of seasonal variability and site-to-site statistics (Fig. 5 and Table 1). Prior CO_2 concentrations overestimate the *in situ* observations at the AMY by about 12 ppm but underestimate at the remote stations

(ULD and GSN) by 2-3 ppm. Prior CH_4 concentrations underestimate at all the stations especially during summer season by 15 ppb. These biases are well matched with uncertainties in the boundary data from the EGG4. The top-down estimates of GHG concentrations show markedly improved agreement with observations relative to the prior, thus demonstrating the efficacy of the EAKF assimilation in adjusting surface GHG concentrations. At the observation locations, the posterior estimates generally fall between the prior and the observations and across all sites and both species, posterior estimates consistently reduce MBE (mean bias error), RMSE (root mean square error) (Table 1). Mean bias of posterior surface CO_2 and CH_4 concentrations are in the range of 1-2 ppm and 20-30 ppb, respectively. The drivers of these improvements vary by site. The largest error reduction for CO_2 occurs at AMY (10.9 ppm), reflecting the correction of the substantial prior overestimation of local emissions from the nearby industrial 'super-cluster' (coal power and petrochemical facilities). In contrast, the largest improvement for CH_4 occurs at GSN (57 ppb), driven principally by the correction of the background bias and the resolution of the latitudinal OH gradient which dominates this southernmost site. Error reductions are most pronounced in summer, consistent with corrections to low-biased boundary inflow for CH_4 and to underrepresented seasonal regional fluxes (e.g., anthropogenic and biogeochemical contributions) when seasonal gradients are largest.

Notable differences are evident in the skewness of the monthly distributions of observed CO_2 and CH_4 concentrations across the sites. At AMY, both prior and posterior CO_2 and CH_4 exhibit strong positive skew and higher variability (elongated upper whiskers in Fig. 5a and 5d), depending on wind around nearby large point sources (i.e., power and industrial plants in the MWI). In contrast, GSN and ULD show more symmetric, compact distributions, suggesting weaker local source influence on these remote stations. All three stations exhibit a pronounced summertime dip in CH_4 concentration, especially in August, consistent with enhanced OH-driven atmospheric oxidation under warm, humid, and high-radiation conditions (East et al., 2024). This seasonal signal is stronger at the lower-latitude sites (AMY, GSN), where oxidation capacity becomes stronger. Similar dips appear in the EGG4 data used as lateral boundary forcing in WRF-Chem GHG (see Fig. S11), indicating that the seasonal CH_4 decline is largely imposed by large scale features.

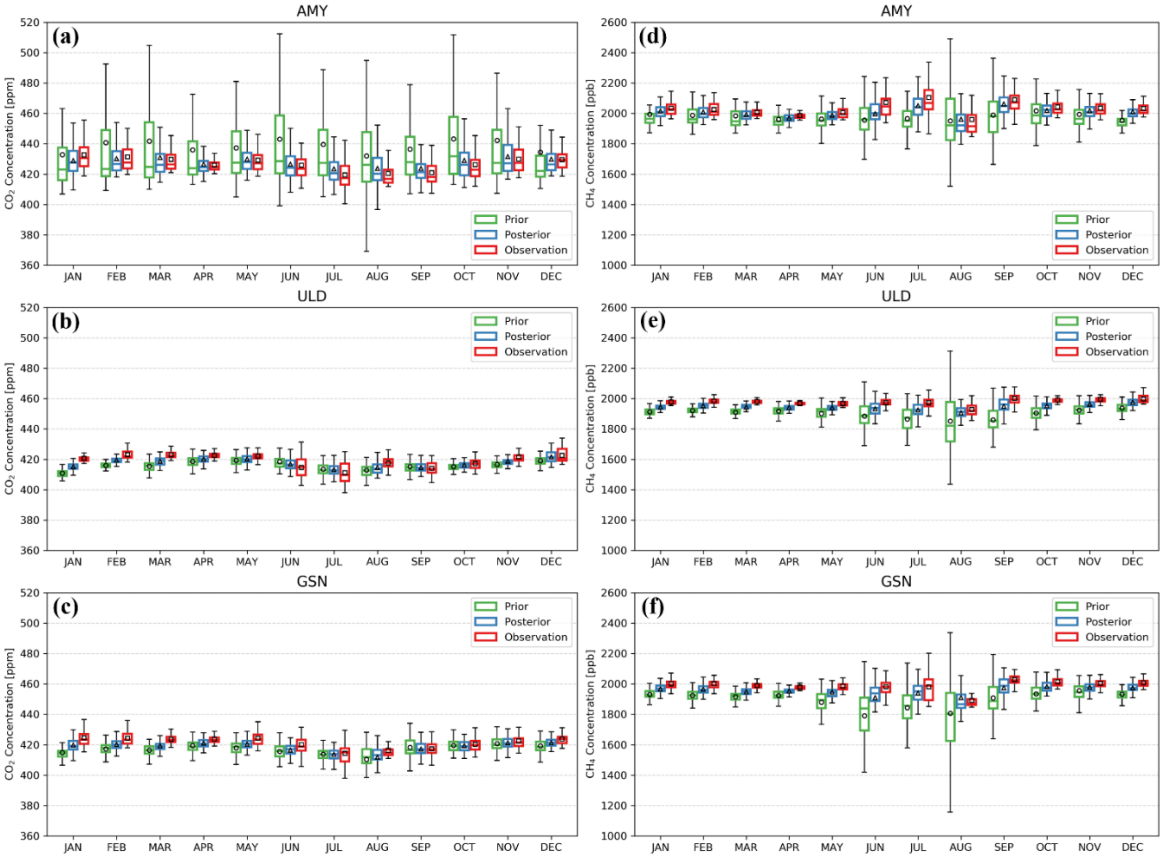

Figure 5. Monthly boxplots of CO_2 (a–c) and CH_4 (d–f) concentrations at AMY (a,d), ULD (b,e), and GSN (c,f) in 2020. Prior (green), posterior (blue), and observations (red) are shown for each site. Boxes denote the interquartile range (25th–75th percentiles); horizontal lines indicate medians. Filled symbols denote means (prior: circle; posterior: triangle; observation: square).

Table 1. Mean bias error (MBE) and root-mean-square error (RMSE of the top-down estimates to the observations at AMY, ULD, and GSN in 2020. Statistics are computed from 6-hourly averages.

Station name	Latitude	Longitude	GHG variable	MBE	RMSE
AMY	36.53°N	126.32°E	Prior CO_2	12.1 ppm	35.2 ppm
			Posterior CO_2	1.2 ppm	13.9 ppm
			Prior CH_4	-52 ppb	163 ppb
			Posterior CH_4	-23 ppb	111 ppb
ULD	37.48°N	130.90°E	Prior CO_2	-2.4 ppm	7.7 ppm
			Posterior CO_2	-1.2 ppm	5.4 ppm

			Prior CH_4	-72 ppb	124 ppb
			Posterior CH_4	-30 ppb	60 ppb
GSN	33.29°N	126.16°E	Prior CO_2	-3.4 ppm	10.0 ppm
			Posterior CO_2	-2.3 ppm	7.4 ppm
			Prior CH_4	-88 ppb	179 ppb
			Posterior CH_4	-31 ppb	109 ppb

7.2 Validation against aircraft observations

To independently evaluate the performance of the inversion system, posterior CO_2 and CH_4 concentrations are compared with aircraft-based *in situ* observations collected over the Yellow Sea near the AMY station in 2020 using a Beechcraft King Air 350. The aircraft was equipped with a CRDS (G2401, Picarro Inc., USA) for measuring CO_2, CH_4, CO, and H_2O, at a sampling rate of 1.5 Hz. Sample air was dried upstream, and inlet ports were located near the front fuselage to minimize contamination. Typical operating altitudes reached 10 km with cruising speeds of 70–120 m s^{-1}, supporting both routine profiling and regional transport characterization. Ten vertical profile flights near the AMY were available in 2020 (not used in the data assimilation) (Fig. S9). After quality control, the profiles were aggregated into 1 km altitude bins (±500 m). Model fields were sampled along the flight track (time-matched and horizontally interpolated to the observation location) and averaged into the same altitude bins. For each bin, we computed mean observed concentrations and observational uncertainties (quadrature of sampling variability and reported measurement uncertainty) alongside the corresponding posterior values.

Figure 6 presents vertical profiles for CO_2 and CH_4 concentrations from both the inversion system and aircraft. Posterior CO_2 concentration is in good agreement with the observed profile with biases of 1-5 ppm even in the upper troposphere, whereas posterior CH_4 concentration profile shows systematic negative bias of 40–50 ppb from the boundary layer to the mid-troposphere. We speculate that this persistent CH_4 bias is a likely combination of residual boundary condition bias in the prescribed CAMS EGG4 inflow mole fraction and under-presented coastal CH_4 sources in prior data over the Yellow Sea. The latter is consistent with the report that shallow shelves and coastal waters can be important CH_4 source regions (Weber et al., 2019; Lee et al., 2018). These results motivate further investigation of maritime CH_4 contributions in the regional prior/boundary treatment and highlight the value of additional observational constraints for improving CH_4 budgets over the Korean Peninsula.

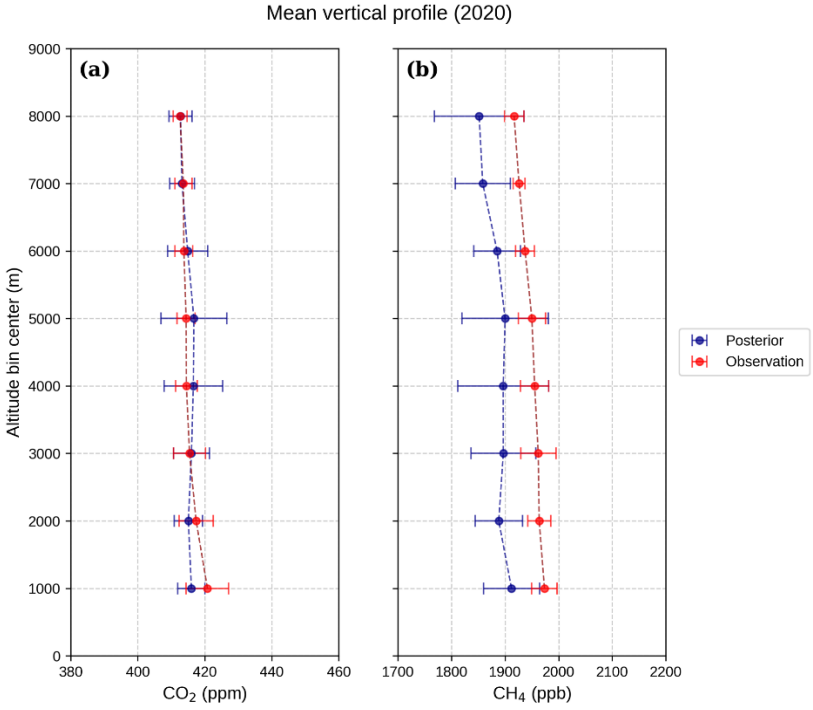

Figure 6. Mean vertical profiles of CO_2 and CH_4 from 10 CM-01 flights over South Korea in 2020. Profiles are aggregated into 1 km altitude bins (±500 m). Symbols and error bars show mean concentrations and associated uncertainties per bin: observations (red) and posterior (blue). Observation uncertainties combine measurement precision and sampling variability.

575

7.3 Uncertainty reduction in concentrations and fluxes

Figures 7 and 8 show the spatial distributions of ensemble spreads for CO_2 and CH_4 concentrations and the corresponding emission uncertainties respectively, showing prior uncertainties (left panels) and uncertainty reductions after the DA (right panels). Unless noted, "reduction" denotes (posterior spread / prior spread − 1) × 100 % over grid cells. Domain-averaged flux
580 uncertainty over land decreases by 25-35 % for CO_2 and about 20 % for CH_4, with local reductions up to 50 % near the observation sites. Prior uncertainties in both concentrations and anthropogenic fluxes are elevated over strong source regions in Seoul Metropolitan Area (SMA), large-scale power plants along the MWI, and the southeastern industrial areas (SCI and SEI) for CO_2. Elevated uncertainties for CH_4 are observed in landfills around the SMA, and rice cultivation area and livestock farms (CLA) (compare Fig. 2 with Fig. 7 and 8). Posterior uncertainties in GHG concentrations decrease substantially within
585 an influence radius of about 90 km (e-folding distance) from all the stations. CH_4 uncertainty reduction reaches up to 40 % around the station and has a larger relative decrease than CO_2. This is consistent with negative bias in CH_4 concentration discussed above. We also note that uncertainty reductions over North Korea and China arise from weak cross-covariances at the range limit; these transboundary updates are not quantitatively interpreted in this study.

The spatial patterns of prior flux uncertainties closely resemble those for concentrations. Overall uncertainties for CO_2 emission decrease by about 7 % after the DA. CO_2 emission uncertainties decrease sharply within the influence radius of the AMY station along the western coasts, particularly for CO_2, where strong anthropogenic GHG sources are located (Fig. 8). Smaller reductions around ULD/GSN (< 5 %) reflect distance from major southeastern sources and prevailing winds. CH_4 emission uncertainties show a similar pattern with that of CO_2 except that the error reduction is relatively smaller than that of CO_2. Posterior flux uncertainty around the AMY shows a relatively smaller reduction in CH_4 compared to CO_2, primarily because major CH_4 sources are located more easterly than those of CO_2. These patterns suggest qualitative priorities for future network expansion (e.g., enhanced CO_2 coverage in the southeastern industrial corridor and CH_4 coverage over central inland hotspots), while noting that a formal network optimization is beyond the scope of this paper. Because the maps are annual means, transient spatial structures at individual cycles are smoothed out; therefore, Figs. 7–10 should be interpreted as persistent features rather than cycle-to-cycle variability, with the strength of sub-national gradients remaining dependent on observational coverage.

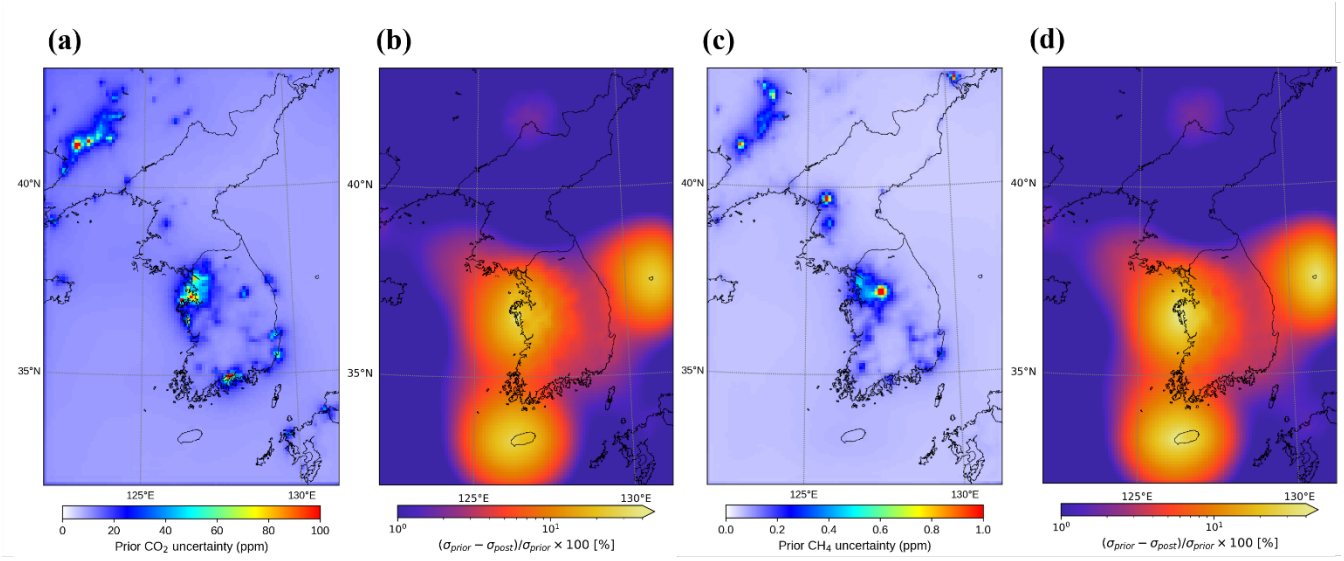

Figure 7. Annual prior concentration uncertainty (ensemble spread) (a,c) and its reduction after assimilation (b,d) for CO_2 (a,b) and CH_4 (c,d) in 2020.

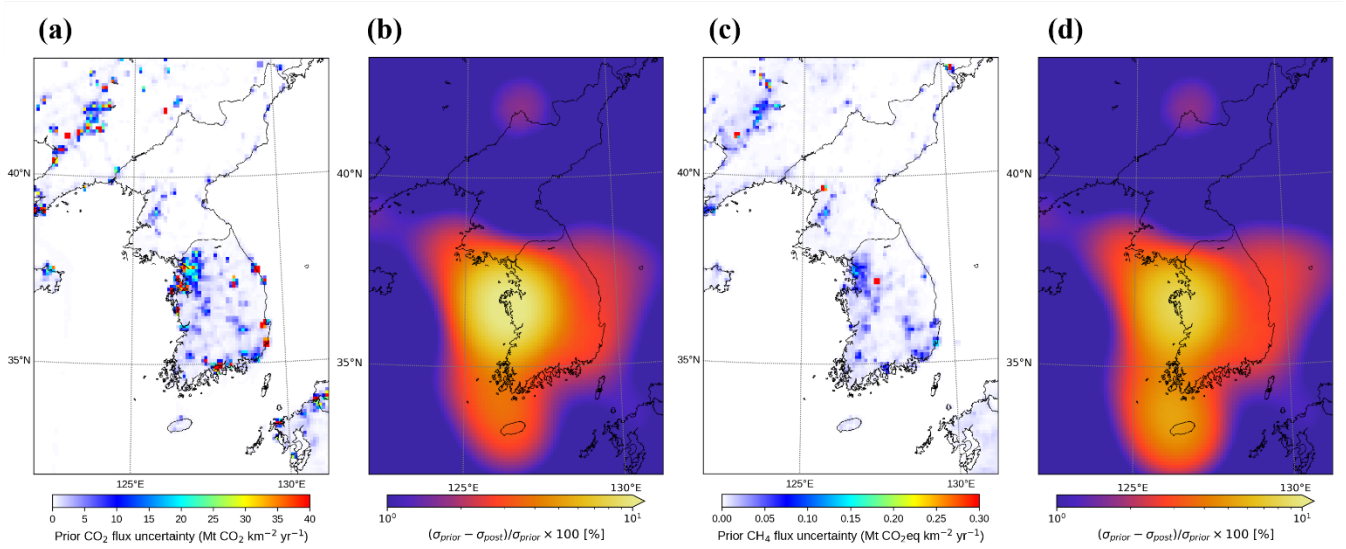

Figure 8. Annual prior flux uncertainty (a and c) and flux-uncertainty reduction (b and d) for CO_2 (a and b) and CH_4 (c and d) in 2020. Note that ocean-grid uncertainties are non-zero but appear small on the plotted scale because the prior spread is prescribed as a fractional perturbation and absolute oceanic flux magnitudes are much smaller than terrestrial sources.

610

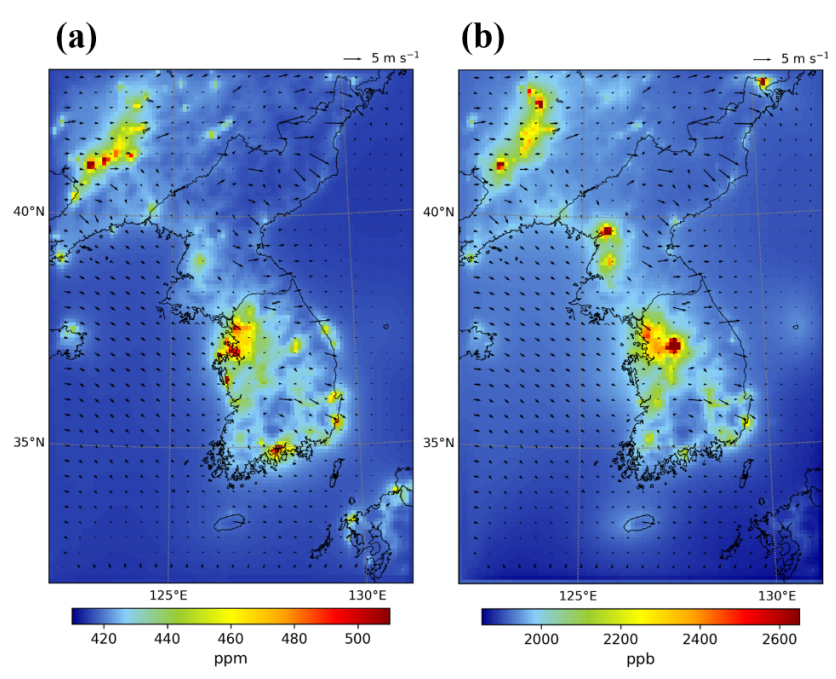

Figure 9. Annual mean surface posterior concentrations of CO_2 (a) and CH_4 (b) over the Korean Peninsula in 2020 from the WRF-Chem/DART inversion system. Wind vectors at 10m illustrate prevailing flow conditions that shape annual concentration gradients.

7.4 Posterior fluxes and concentrations of CO_2 and CH_4

Figures 9 shows spatial distribution of CO_2 and CH_4 concentrations from the inversion system. Posterior GHG concentrations capture large-scale gradients and regional enhancements induced by both long-range transport and upwind source regions. Elevated concentrations are clearly identified over key heavy industry and dense urban zones, specifically along the SMA, the west coast, and the southern industrial corridor (MWI, SCI, and SEI; Fig. 2b) for CO_2. In contrast, enhanced CH_4 concentrations are more closely associated with agricultural and waste-related source regions, including central–western Korea and the CLA region (Fig. 2c). When viewed alongside CAMS EGG4, both fields exhibit the broad synoptic structures, including persistent enhancements over the western Korean Peninsula and eastern China and the seasonal cycle of winter accumulation and summer dilution (Figs. S10–S13). However, the structural differences between the two products primarily reflect differences in resolution and representation, highlighting the benefit of the high-resolution regional framework for sub-national patterns. While EGG4 depicts spatially smoother concentration fields characteristic of its coarser global resolution ($0.75° \times 0.75°$) the posterior estimates resolve sharper gradients and more distinct hotspots over major source regions such as the SMA and MWI (Figs. 9 and S14a). Similarly, elevated CH_4 concentrations over the CLA are resolved as more localized features in the posterior, whereas these appear as broader, more diffuse patterns in the global product. These features are consistent with previous studies based on satellite products of the GOSAT and TROPOMI (Shim et al., 2019; Moon et al., 2024), which noted that coarse-resolution global products tend to smooth out fine-scale urban–industrial heterogeneity. These results illustrate a high-resolution regional inversion represent fine-scale spatial gradients and localized source-region signatures that are often averaged out at coarser global scales when it combines local priors, mesoscale meteorology, and continuous in situ observations.

Figure 10 summarizes the posterior anthropogenic flux fields and the spatial distribution of flux adjustments (posterior minus prior). The overall spatial patterns of posterior CO_2 and CH_4 emissions remain similar to the priors, retaining the major hotspots over the Korean Peninsula (Fig. 2b and 2c), as expected given the current observing network and the use of covariance localization. Spatially varying posterior adjustments are nonetheless produced to reduce concentration innovations at the observation sites. With the current observation configuration, these adjustments are best interpreted as regionally coherent corrections within the localization-supported influence region, while finer-scale structure remains strongly constrained by the prior and the assumed error statistics. Negative increments of CO_2 emissions are concentrated in densely populated and traffic-heavy regions (SMA and MWI) and positive increments for CO_2 emission are observed along the east coast and in the southeastern industrial corridor (i.e., SCI and SEI) (Fig. 10b). These patterns are broadly consistent with the sign of the station-based concentration biases (Table 1) and suggest that innovations at AMY (positive bias) tend to project onto nearby western source regions as flux reductions, whereas innovations at GSN and ULD (negative bias) can contribute to increased fluxes in the southern/eastern industrial regions through localized concentration–flux covariances. This behavior may also reflect sector-dependent structural uncertainties in the priors, given the strong contribution of heavy industry (steel, petrochemical,

shipbuilding, vehicle manufacturing) in SCI and SEI relative to the more mixed urban/energy source mix in SMA/MWI. Positive increments for CH_4 emission are widespread across inland source regions associated with rice paddy, livestock facilities, landfills, and power-industry (Fig. 10d). Given the persistent negative CH_4 bias in the independent aircraft profiles (Section 7.2), we interpret these increases with caution because of the possibility for compensation for low-biased prescribed boundary mole fractions. At the same time, the spatial correspondence with known inland hotspots suggests that missing or underestimated sources in the prior may also contribute. Further work is therefore needed to disentangle boundary-condition bias, transport/representativeness error, and prior source errors, including sensitivity tests using alternative boundary products and expanded observational constraints (e.g., additional in situ and upper-air measurements).

Figure 11 compares national-total anthropogenic CO_2 and CH_4 emissions for South Korea in 2020 from the posterior with multiple bottom-up inventories. For CO_2, the comparison encompasses Open-source Data Inventory for Anthropogenic CO_2 (ODIAC) (Oda et al., 2018), the Fossil Fuel Data Assimilation System (FFDAS) (Rayner et al., 2010), the Gridded Daily Fossil CO_2 Emissions Dataset (GRACED) (Dou et al., 2023), EDGAR, and the national total anthropogenic emissions (excluding the LULUCF sector) as reported in the Biennial Transparent Report of the Republic of Korea (ROK-BTR, hereafter). Because these products differ substantially in scope and construction (e.g., fossil-fuel-only versus IPCC-sector totals), proxy choice, point-source treatment, spatial disaggregation, native resolution, and sector attribution, we interpret the comparison as a consistency check under a harmonized scope (anthropogenic CO_2 excluding LULUCF) rather than as a validation target (Hutchins et al., 2017). Under the harmonized scope and spatial aggregation used here, EDGAR's national-total anthropogenic CO_2 is most consistent with the ROK-BTR estimate among the bottom-up datasets considered. EDGAR is the closest to ROK-BTR (4% higher), whereas FFDAS, GRACED, and ODIAC deviate more than EDGAR (from about -31%, to10%). In 2020, our posterior CO_2 total is broadly consistent with ROK-BTR at the national scale (Fig. 11). In contrast, posterior CH_4 total shows weaker agreement with the available bottom-up estimates, consistent with the larger structural uncertainty in CH_4 source characterization and spatial allocation noted in previous studies (e.g., Moon et al., 2024).

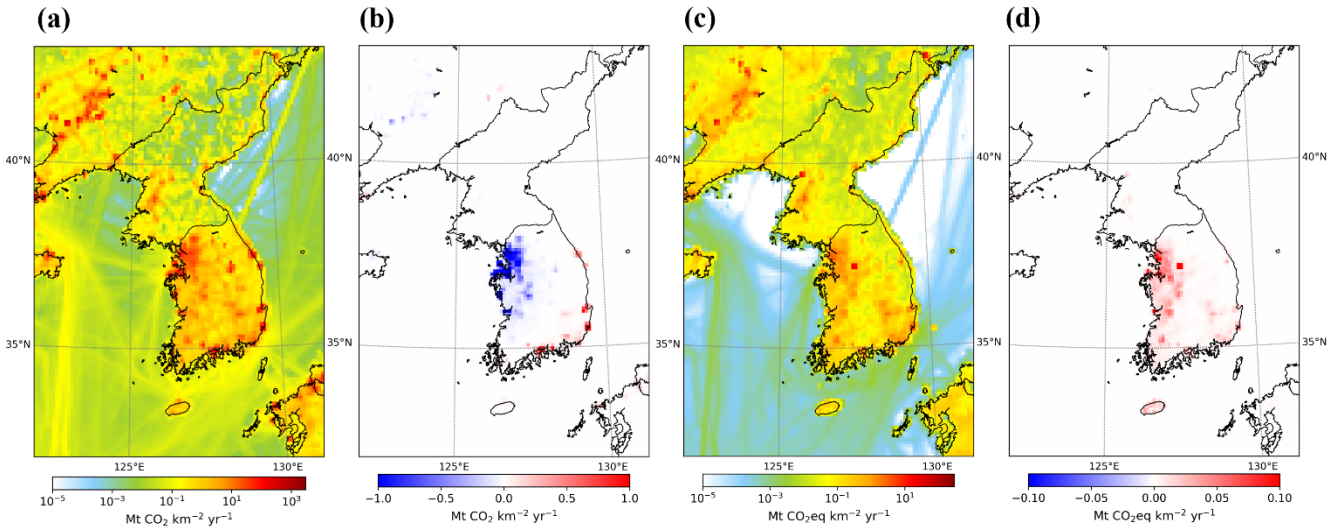

Figure 10. Annual-mean posterior surface fluxes (a and c) and assimilation increments (posterior minus prior) (b and d) for CO_2 (a and b) and CH_4 (c and d) from the WRF-Chem/DART system. Red (blue) shading indicates an increase (decrease) in the posterior relative to the prior.

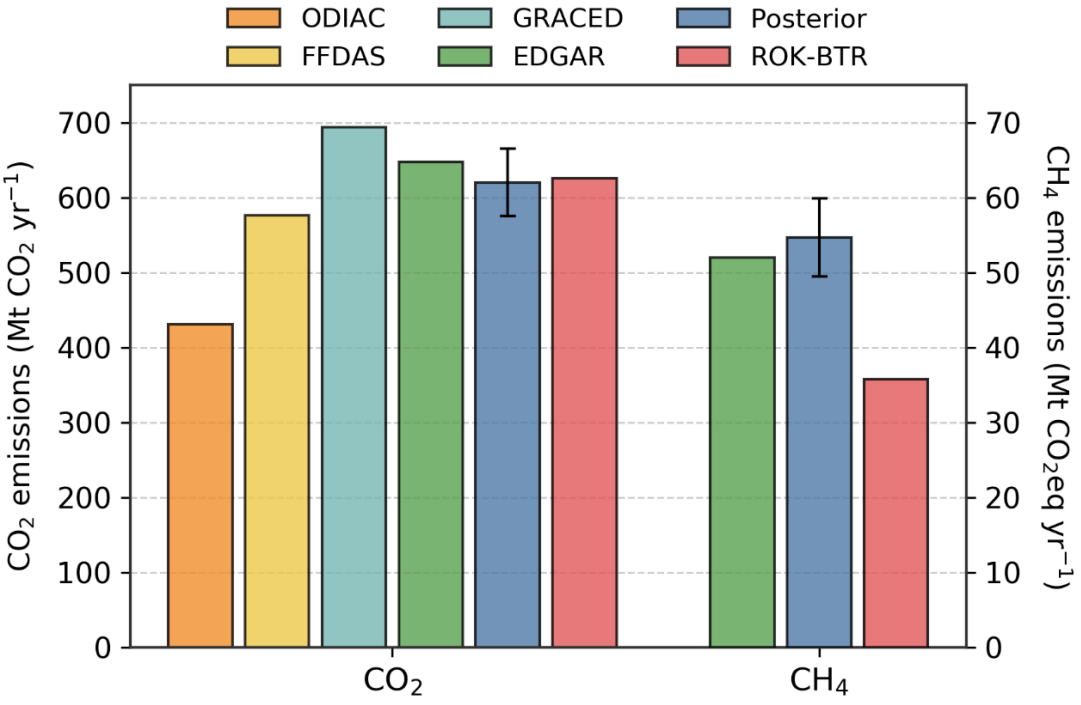

Figure 11. Annual total anthropogenic CO_2 and CH_4 emissions over South Korea in 2020 from multiple datasets. CO_2 comparisons include ODIAC, FFDAS, GRACED, EDGAR, ROK-BTR, and the posterior (six sources). CH_4 comparisons include EDGAR, ROK-BTR, and the posterior. Error bars denote posterior uncertainty. (FFDAS was scaled using the 2015–2020 gross emission growth rate from ROK-BTR because FFDAS is available only through 2015)

8 Summary and Conclusion

This study presents a high-resolution dual-species GHG (CO_2 and CH_4) inversion framework using the coupled WRF-Chem/DART system, which assimilates continuous high-precision *in situ* observations of GHG concentrations. The system provides transport-consistent and observation-constrainaed emission estimates and dynamically consistent temporal state updates through ensemble data assimilation. By coupling meteorology and tracer transport and updating both meteorological and tracer states within the cycling system, the framework supports internally consistent transport-concentration-flux adjustments over complex terrain. The incorporation of precise high-frequency *in situ* observations further helps better representation of near-surface gradients, thereby enhancing anthropogenic flux sensitivity.

This framework is designed to accommodate denser and more diverse observing systems (e.g., additional surface sites, tall towers, aircraft profiles, and satellite column retrievals) within the same data-assimilation framework; although extending to various types of observations may involve implementing the corresponding observation operators and specifying observation-error/representativeness settings (including bias treatment where applicable), together with network-dependent tuning (e.g., localization and observation error) as needed. A compact controlled twin experiment with synthetic observations from an expanded 50-site surface network illustrates how emission constraints strengthen as observational density increases, clarifying the expected direction and spatial structure of uncertainty reduction and informing iterative inventory refinement.

Our Eulerian dual-state EAKF framework provides a more integrated and internally consistent treatment of background errors and filter stability within a cycling joint state–parameter assimilation system for GHG concentrations and emissions, compared with footprint-based Lagrangian inversions. Because meteorology and 3-D tracer fields are advanced and analyzed within the same model, background-error covariances are represented in a flow-dependent manner by the evolving ensemble, rather than being prescribed a priori via static spatial correlations or fixed regularization operators that are often adopted in footprint-based approaches. In addition, the DART configuration provides an explicit, principled inflation framework to maintain physically plausible ensemble spread and to mitigate ensemble collapse during repeated cycling, offering a systematic handle on under-dispersion arising from unresolved transport/model errors and finite-ensemble sampling. By contrast, typical Lagrangian inversions typically manage under-dispersive behavior implicitly through tuning of prior error magnitudes, prescribed covariance structures, or regularization strength, without an inflation mechanism that is directly coupled to sequential filter dynamics. These advantages come with trade-offs. Running an ensemble is computationally more expensive than footprint calculations, posterior updates depend on the fidelity of the underlying meteorological and sub-grid physical parameterizations that govern transport and mixing.

In the 2020 real-data application, the system reduces mismatches with observed CO_2 and CH_4 at all high-precision sites and yields posterior uncertainty reduction in both concentrations and emissions. The posterior surface biases (1.2 ppm for CO_2 and 30 ppb for CH_4 over 2020) are smaller than those implied by the prescribed CAMS EGG4 IC/BC forcing at the surface observatory, indicating improved consistency with local observations under the cycling configuration. National totals are broadly consistent with the Republic of Korea inventory under the defined scope, while showing regionally varying

adjustments relative to the prior over densely populated, industrial, and agricultural areas. Posterior increments suggest that prior CO_2 emissions may be overestimated over the Seoul Metropolitan Area and portions of the western coastal region, whereas CH_4 emissions may be underestimated over inland agricultural hotspots; CH_4 adjustments should be interpreted with caution given the potential sensitivity to boundary-condition biases and maritime source representation. These results underscore the value of top-down constraints for sub-national inventory refinement and for an aggregate-level consistency check. To our knowledge, this study provides the first fully documented regional WRF-Chem/DART workflow for simultaneous CO_2 and CH_4 estimation within a cycling dual-state configuration at kilometer-scale resolution, combining in situ GHG assimilation with meteorological data assimilation. Overall, this high-resolution dual-species WRF-Chem/DART inversion framework leveraging surface heterogeneity-aware parameterizations provides a practical basis for spatially explicit emission analyses that support policy applications, operational monitoring, and MMRV-oriented verification at national and sub-national scales.

Code and Data availability

Model source code used in this study are archived on Zenodo under https://doi.org/10.5281/zenodo.16939122 (Kwon et al., 2025a). Preprocessed data, model output, and model configurations used in this study are archived on Zenodo under https://doi.org/10.5281/zenodo.16947463 (Kwon et al., 2025b). ERA5 is available after registration at https://doi.org/10.24381/cds.adbb2d47 (pressure levels) (Hersbach et al., 2023a) and https://doi.org/10.24381/cds.bd0915c6 (single level) (Hersbach et al., 2023b). CAMS EGG4 is available after registration at https://doi.org/10.24381/cda4ed31 (Copernicus Atmosphere Monitoring Service, 2022). PREPBUFR is available at https://doi.org/10.5065/Z83F-N512 (National Centers for Environmental Prediction, 2008). EDGARv8.0 is available at https://edgar.jrc.ec.europa.eu/dataset_ghg80 (Crippa et al., 2023). FFDAS is available at https://ffdas.rc.nau.edu/Data.html (Rayner et al., 2010). GRACED is available after registration at https://carbonmonitor-graced.com (Dou et al., 2023). ODIAC is available at https://doi.org/10.17595/20170411.001 (Oda et al., 2015). FINNv2.5 is available after registration at https://doi.org/10.5065/XNPA-AF09 (Wiedinmyer and Emmons, 2022). SeaFlux is available at https://doi.org/10.5281/zenodo.5482547 (Gregor and Fay, 2021). Annual budget of CO_2 and CH_4 emissions in South Korea is available under https://unfccc.int/documents/645637 (Biennial Transparency Report of Republic of Korea, 2025). EDGARv8.0, FFDAS, GRACED and the Republic of Korea's Biennial Transparency Report are also archived on Zenodo under https://doi.org/10.5281/zenodo.17402804 (Kwon et al., 2025c). Access to the repositories archived on Zenodo will be provided upon request to the corresponding author.

Author contributions

DK, BK, ES, AA, CS, DS, SK, SJ, and JH conceptualized and designed the study. DK, BK, JL, JK, ES, and AA contributed to the implementation and development of the forward and inverse modeling framework. DS, SL, SK, and SJ were responsible for the WMO/GAW KMA observation program and the aircraft-based measurement. DK and JA performed preprocessing and visualization of the VPRM inputs and outputs. DK and BK collected and processed the remaining input datasets, conducted the model simulations, and carried out the analysis and visualization. DK, BK, and JH prepared the original draft. All authors reviewed and edited the manuscript.

Competing interests

One of the authors is a member of the editorial board of Geoscientific Model Development.

Acknowledgements

We sincerely thank the editor, staffs, and all the reviewers for their constructive comments and support, which significantly improved this paper. We received help from an AI tool for English improvement.

Financial support

This work was funded by the Korea Meteorological Administration Research and Development Program under Grant RS-2024-00404365.

References

Agustí-Panareda, A., Barré, J., Massart, S., Inness, A., Aben, I., Ades, M., Baier, B. C., Balsamo, G., Borsdorff, T., Bousserez, N., Boussetta, S., Buchwitz, M., Cantarello, L., Crevoisier, C., Engelen, R., Eskes, H., Flemming, J., Garrigues, S., Hasekamp, O., Huijnen, V., Jones, L., Kipling, Z., Langerock, B., McNorton, J., Meilhac, N., Noël, S., Parrington, M., Peuch, V.-H., Ramonet, M., Razinger, M., Reuter, M., Ribas, R., Suttie, M., Sweeney, C., Tarniewicz, J., and Wu, L.: Technical note: The CAMS greenhouse gas reanalysis from 2003 to 2020, Atmospheric Chemistry and Physics, 23, 3829–3859, https://doi.org/10.5194/acp-23-3829-2023, 2023.

Ahmadov, R., Gerbig, C., Kretschmer, R., Koerner, S., Neininger, B., Dolman, A. J., and Sarrat, C.: Mesoscale covariance of transport and CO2 fluxes: Evidence from observations and simulations using the WRF-VPRM coupled atmosphere-biosphere model, Journal of Geophysical Research: Atmospheres, 112, https://doi.org/10.1029/2007JD008552, 2007.

Anderson, J., Hoar, T., Raeder, K., Liu, H., Collins, N., Torn, R., and Avellano, A.: The Data Assimilation Research Testbed: A Community Facility, Bulletin of the American Meteorological Society, 90, 1283–1296, https://doi.org/10.1175/2009BAMS2618.1, 2009.

Anderson, J. L.: An Ensemble Adjustment Kalman Filter for Data Assimilation, Monthly Weather Review, 129, 2884–2903, https://doi.org/10.1175/1520-0493(2001)129<2884:AEAKFF>2.0.CO;2, 2001.

Anderson, J. L.: A Local Least Squares Framework for Ensemble Filtering, Monthly Weather Review, 131, 634–642, https://doi.org/10.1175/1520-0493(2003)131%253C0634:ALLSFF%253E2.0.CO;2, 2003.

Anderson, J. L.: Localization and Sampling Error Correction in Ensemble Kalman Filter Data Assimilation, Monthly Weather Review, 140, 2359–2371, https://doi.org/10.1175/MWR-D-11-00013.1, 2012.

Barker, D., Huang, X.-Y., Liu, Z., Auligné, T., Zhang, X., Rugg, S., Ajjaji, R., Bourgeois, A., Bray, J., Chen, Y., Demirtas, M., Guo, Y.-R., Henderson, T., Huang, W., Lin, H.-C., Michalakes, J., Rizvi, S., and Zhang, X.: The Weather Research and Forecasting Model's Community Variational/Ensemble Data Assimilation System: WRFDA, Bulletin of the American Meteorological Society, 93, 831–843, https://doi.org/10.1175/BAMS-D-11-00167.1, 2012.

Beck, V., Koch, T., Kretschmer, R., Marshall, J.and Ahmadov, R., Gerbig, C., Pillai, D., and Heimann, M.: The WRF Greenhouse Gas Model (WRF-GHG). Technical Report No. 25, Tech. rep., Max Planck Institute for Biogeochemistry, Jena, Germany, https://www.bgc-jena.mpg.de/5363366/tech_report25.pdf, 2012.

Biennial Transparency Report of Republic of Korea [data set], https://unfccc.int/documents/645637 (last access: 22 October 2025), 2025.

Brunner, D., Suter, I., Bernet, L., Constantin, L., Grange, S. K., Rubli, P., Li, J., Chen, J., Bigi, A., and Emmenegger, L.: Building-resolving simulations of anthropogenic and biospheric CO_2 in the city of Zurich with GRAMM/GRAL, EGUsphere, 1–34, https://doi.org/10.5194/egusphere-2025-640, 2025.

Bukosa, B., Mikaloff-Fletcher, S., Brailsford, G., Smale, D., Keller, E. D., Baisden, W. T., Kirschbaum, M. U. F., Giltrap, D. L., Liáng, L., Moore, S., Moss, R., Nichol, S., Turnbull, J., Geddes, A., Kennett, D., Hidy, D., Barcza, Z., Schipper, L. A.,

Wall, A. M., Nakaoka, S.-I., Mukai, H., and Brandon, A.: Inverse modelling of New Zealand's carbon dioxide balance estimates a larger than expected carbon sink, EGUsphere, 1–41, https://doi.org/10.5194/egusphere-2024-3866, 2025.

Bréon, F. M., Broquet, G., Puygrenier, V., Chevallier, F., Xueref-Remy, I., Ramonet, M., Dieudonné, E., Lopez, M., Schmidt, M., Perrussel, O., and Ciais, P.: An attempt at estimating Paris area CO_2 emissions from atmospheric concentration measurements, Atmospheric Chemistry and Physics, 15, 1707–1724, https://doi.org/10.5194/acp-15-1707-2015, 2015.

Byrne, B., Baker, D. F., Basu, S., Bertolacci, M., Bowman, K. W., Carroll, D., Chatterjee, A., Chevallier, F., Ciais, P., Cressie, N., Crisp, D., Crowell, S., Deng, F., Deng, Z., Deutscher, N. M., Dubey, M. K., Feng, S., García, O. E., Griffith, D. W. T., Herkommer, B., Hu, L., Jacobson, A. R., Janardanan, R., Jeong, S., Johnson, M. S., Jones, D. B. A., Kivi, R., Liu, J., Liu, Z., Maksyutov, S., Miller, J. B., Miller, S. M., Morino, I., Notholt, J., Oda, T., O'Dell, C. W., Oh, Y.-S., Ohyama, H., Patra, P. K., Peiro, H., Petri, C., Philip, S., Pollard, D. F., Poulter, B., Remaud, M., Schuh, A., Sha, M. K., Shiomi, K., Strong, K., Sweeney, C., Té, Y., Tian, H., Velazco, V. A., Vrekoussis, M., Warneke, T., Worden, J. R., Wunch, D., Yao, Y., Yun, J., Zammit-Mangion, A., and Zeng, N.: National CO_2 budgets (2015–2020) inferred from atmospheric CO_2 observations in support of the global stocktake, Earth System Science Data, 15, 963–1004, https://doi.org/10.5194/essd-15-963-2023, 2023.

Callewaert, S., Brioude, J., Langerock, B., Duflot, V., Fonteyn, D., Müller, J.-F., Metzger, J.-M., Hermans, C., Kumps, N., Ramonet, M., Lopez, M., Mahieu, E., and De Mazière, M.: Analysis of CO_2, CH_4, and CO surface and column concentrations observed at Réunion Island by assessing WRF-Chem simulations, Atmospheric Chemistry and Physics, 22, 7763–7792, https://doi.org/10.5194/acp-22-7763-2022, 2022.

Callewaert, S.: WRF-GHG user guide, Royal Belgian Institute for Space Aeronomy (BIRA-IASB), https://doi.org/10.18758/Q6RAPNEU, 2024.

Copernicus Atmosphere Monitoring Service: CAMS global greenhouse gas reanalysis (EGG4), CAMS Atmosphere Data Store (ADS) [data set], https://doi.org/10.24380/8fck-9w87 (last access: 22 October 2025), 2021.

Crippa, M., Guizzardi D., Pagani F., Banja M., Muntean M., Schaaf E., Becker, W., Monforti-Ferrario F., Quadrelli, R., Risquez Martin, A., Taghavi-Moharamli, P., Grassi, G., Rossi, S., Brandao De Melo, J., Oom, D., Branco, A., San-Miguel, J., Vignati, E.: EDGAR v8.0 Greenhouse Gas Emissions, European Commission, Joint Research Centre (JRC) [data set] https://doi.org/10.2905/b54d8149-2864-4fb9-96b9-5fd3a020c224 (last access: 22 October 2025), 2023

Crippa, M., Guizzardi, D., Pagani, F., Schiavina, M., Melchiorri, M., Pisoni, E., Graziosi, F., Muntean, M., Maes, J., Dijkstra, L., Van Damme, M., Clarisse, L., and Coheur, P.: Insights into the spatial distribution of global, national, and subnational greenhouse gas emissions in the Emissions Database for Global Atmospheric Research (EDGAR v8.0), Earth System Science Data, 16, 2811–2830, https://doi.org/10.5194/essd-16-2811-2024, 2024.

Custódio, D., Borrego, C., and Relvas, H.: Worldwide evaluation of CAMS-EGG4 CO_2 data re-analysis at the surface level, Toxics, 10, 331, https://doi.org/10.3390/toxics10060331, 2022.

Dekker, I. N., Houweling, S., Aben, I., Röckmann, T., Krol, M., Martínez-Alonso, S., Deeter, M. N., and Worden, H. M.: Quantification of CO emissions from the city of Madrid using MOPITT satellite retrievals and WRF simulations, Atmospheric Chemistry and Physics, 17, 14675–14694, https://doi.org/10.5194/acp-17-14675-2017, 2017.

Deng, Z., Ciais, P., Tzompa-Sosa, Z. A., Saunois, M., Qiu, C., Tan, C., Sun, T., Ke, P., Cui, Y., Tanaka, K., Lin, X., Thompson, R. L., Tian, H., Yao, Y., Huang, Y., Lauerwald, R., Jain, A. K., Xu, X., Bastos, A., Sitch, S., Palmer, P. I., Lauvaux, T., d'Aspremont, A., Giron, C., Benoit, A., Poulter, B., Chang, J., Petrescu, A. M. R., Davis, S. J., Liu, Z., Grassi, G., Albergel, C., Tubiello, F. N., Perugini, L., Peters, W., and Chevallier, F.: Comparing national greenhouse gas budgets reported in UNFCCC inventories against atmospheric inversions, Earth System Science Data, 14, 1639–1675, https://doi.org/10.5194/essd-14-1639-2022, 2022.

Denison, S., Forster, P. M., and Smith, C. J.: Guidance on emissions metrics for nationally determined contributions under the Paris Agreement, Environ. Res. Lett., 14, 124002, https://doi.org/10.1088/1748-9326/ab4df4, 2019.

Dou, X., Hong, J., Ciais, P., Chevallier, F., Yan, F., Yu, Y., Hu, Y., Huo, D., Sun, Y., Wang, Y., Davis, S. J., Crippa, M., Janssens-Maenhout, G., Guizzardi, D., Solazzo, E., Lin, X., Song, X., Zhu, B., Cui, D., Ke, P., Wang, H., Zhou, W., Huang, X., Deng, Z., and Liu, Z.: Near-real-time global gridded daily CO_2 emissions 2021, Sci Data, 10, 69, https://doi.org/10.1038/s41597-023-01963-0, 2023.

East, J. D., Jacob, D. J., Balasus, N., Bloom, A. A., Bruhwiler, L., Chen, Z., Kaplan, J. O., Mickley, L. J., Mooring, T. A., Penn, E., Poulter, B., Sulprizio, M. P., Worden, J. R., Yantosca, R. M., and Zhang, Z.: Interpreting the Seasonality of Atmospheric Methane, Geophysical Research Letters, 51, e2024GL108494, https://doi.org/10.1029/2024GL108494, 2024.

Elguindi, N., Granier, C., Stavrakou, T., Darras, S., Bauwens, M., Cao, H., Chen, C., Denier Van Der Gon, H. A. C., Dubovik, O., Fu, T. M., Henze, D. K., Jiang, Z., Keita, S., Kuenen, J. J. P., Kurokawa, J., Liousse, C., Miyazaki, K., Müller, J.-F., Qu, Z., Solmon, F., and Zheng, B.: Intercomparison of Magnitudes and Trends in Anthropogenic Surface Emissions From Bottom-Up Inventories, Top-Down Estimates, and Emission Scenarios, Earth's Future, 8, e2020EF001520, https://doi.org/10.1029/2020EF001520, 2020.Enting, I. G.: Inverse Problems in Atmospheric Constituent Transport, Cambridge University Press, Cambridge, https://doi.org/10.1017/CBO9780511535741, 2002.

Fay, A. R., Gregor, L., Landschützer, P., McKinley, G. A., Gruber, N., Gehlen, M., Iida, Y., Laruelle, G. G., Rödenbeck, C., Roobaert, A., and Zeng, J.: SeaFlux: harmonization of air–sea CO_2 fluxes from surface pCO_2 data products using a standardized approach, Earth System Science Data, 13, 4693–4710, https://doi.org/10.5194/essd-13-4693-2021, 2021.

Feng, S., Lauvaux, T., Davis, K. J., Keller, K., Zhou, Y., Williams, C., Schuh, A. E., Liu, J., and Baker, I.: Seasonal Characteristics of Model Uncertainties From Biogenic Fluxes, Transport, and Large-Scale Boundary Inflow in Atmospheric CO_2 Simulations Over North America, Journal of Geophysical Research: Atmospheres, 124, 14325–14346, https://doi.org/10.1029/2019JD031165, 2019.

Friedlingstein, P., O'Sullivan, M., Jones, M. W., Andrew, R. M., Hauck, J., Landschützer, P., Le Quéré, C., Li, H., Luijkx, I. T., Olsen, A., Peters, G. P., Peters, W., Pongratz, J., Schwingshackl, C., Sitch, S., Canadell, J. G., Ciais, P., Jackson, R. B., Alin, S. R., Arneth, A., Arora, V., Bates, N. R., Becker, M., Bellouin, N., Berghoff, C. F., Bittig, H. C., Bopp, L., Cadule,

P., Campbell, K., Chamberlain, M. A., Chandra, N., Chevallier, F., Chini, L. P., Colligan, T., Decayeux, J., Djeutchouang, L. M., Dou, X., Duran Rojas, C., Enyo, K., Evans, W., Fay, A. R., Feely, R. A., Ford, D. J., Foster, A., Gasser, T., Gehlen, M., Gkritzalis, T., Grassi, G., Gregor, L., Gruber, N., Gürses, Ö., Harris, I., Hefner, M., Heinke, J., Hurtt, G. C., Iida, Y., Ilyina, T., Jacobson, A. R., Jain, A. K., Jarníková, T., Jersild, A., Jiang, F., Jin, Z., Kato, E., Keeling, R. F., Klein Goldewijk, K., Knauer, J., Korsbakken, J. I., Lan, X., Lauvset, S. K., Lefèvre, N., Liu, Z., Liu, J., Ma, L., Maksyutov, S., Marland, G., Mayot, N., McGuire, P. C., Metzl, N., Monacci, N. M., Morgan, E. J., Nakaoka, S.-I., Neill, C., Niwa, Y., Nützel, T., Olivier, L., Ono, T., Palmer, P. I., Pierrot, D., Qin, Z., Resplandy, L., Roobaert, A., Rosan, T. M., Rödenbeck, C., Schwinger, J., Smallman, T. L., Smith, S. M., Sospedra-Alfonso, R., Steinhoff, T., Sun, Q., Sutton, A. J., Séférian, R., Takao, S., Tatebe, H., Tian, H., Tilbrook, B., Torres, O., Tourigny, E., Tsujino, H., Tubiello, F., van der Werf, G., Wanninkhof, R., Wang, X., Yang, D., Yang, X., Yu, Z., Yuan, W., Yue, X., Zaehle, S., Zeng, N., and Zeng, J.: Global Carbon Budget 2024, Earth Syst. Sci. Data, 17, 965–1039, https://doi.org/10.5194/essd-17-965-2025, 2025.

Gaspari, G. and Cohn, S. E.: Construction of correlation functions in two and three dimensions, Quarterly Journal of the Royal Meteorological Society, 125, 723–757, https://doi.org/10.1002/qj.49712555417, 1999.

Gaudet, B. J., Davis, K. J., Pal, S., Jacobson, A. R., Schuh, A., Lauvaux, T., Feng, S., and Browell, E. V.: Regional-Scale, Sector-Specific Evaluation of Global CO_2 Inversion Models Using Aircraft Data From the ACT-America Project, Journal of Geophysical Research: Atmospheres, 126, e2020JD033623, https://doi.org/10.1029/2020JD033623, 2021.

Gregor, L. and Fay, A.: SeaFlux: harmonised sea-air CO2 fluxes from surface pCO_2 data products using a standardised approach (2021.04.03), [data set], https://doi.org/10.5281/zenodo.5482547 (last access: 22 October 2025), 2021.

Grell, G. A., Peckham, S. E., Schmitz, R., McKeen, S. A., Frost, G., Skamarock, W. C., and Eder, B.: Fully coupled "online" chemistry within the WRF model, Atmospheric Environment, 39, 6957–6975, https://doi.org/10.1016/j.atmosenv.2005.04.027, 2005.

Gurney, K. R., Law, R. M., Denning, A. S., Rayner, P. J., Baker, D., Bousquet, P., Bruhwiler, L., Chen, Y.-H., Ciais, P., Fan, S., Fung, I. Y., Gloor, M., Heimann, M., Higuchi, K., John, J., Maki, T., Maksyutov, S., Masarie, K., Peylin, P., Prather, M., Pak, B. C., Randerson, J., Sarmiento, J., Taguchi, S., Takahashi, T., and Yuen, C.-W.: Towards robust regional estimates of CO_2 sources and sinks using atmospheric transport models, Nature, 415, 626–630, https://doi.org/10.1038/415626a, 2002.

Harman, I. N.: The Role of Roughness Sublayer Dynamics Within Surface Exchange Schemes, Boundary-Layer Meteorol, 142, 1–20, https://doi.org/10.1007/s10546-011-9651-z, 2012.

Harman, I. N. and Finnigan, J. J.: A simple unified theory for flow in the canopy and roughness sublayer, Boundary-Layer Meteorol, 123, 339–363, https://doi.org/10.1007/s10546-006-9145-6, 2007.

Harman, I. N. and Finnigan, J. J.: Scalar Concentration Profiles in the Canopy and Roughness Sublayer, Boundary-Layer Meteorol, 129, 323–351, https://doi.org/10.1007/s10546-008-9328-4, 2008.

Henne, S., Brunner, D., Oney, B., Leuenberger, M., Eugster, W., Bamberger, I., Meinhardt, F., Steinbacher, M., and Emmenegger, L.: Validation of the Swiss methane emission inventory by atmospheric observations and inverse modelling, Atmospheric Chemistry and Physics, 16, 3683–3710, https://doi.org/10.5194/acp-16-3683-2016, 2016.

Hersbach, H., Bell, B., Berrisford, P., Biavati, G., Horányi, A., Muñoz Sabater, J., Nicolas, J., Peubey, C., Radu, R., Rozum, I., Schepers, D., Simmons, A., Soci, C., Dee, D., and Thépaut, J.-N.: ERA5 hourly data on pressure levels from 1959 to present, Copernicus Climate Change Service (C3S) Climate Data Store (CDS) [data set], https://doi.org/10.24381/cds.bd0915c6 (last access: 22 October 2025), 2023a.

Hersbach, H., Bell, B., Berrisford, P., Biavati, G., Horányi, A., Muñoz Sabater, J., Nicolas, J., Peubey, C., Radu, R., Rozum, I., Schepers, D., Simmons, A., Soci, C., Dee, D., and Thépaut, J.-N.: ERA5 hourly data on single levels from 1959 to present, Copernicus Climate Change Service (C3S) Climate Data Store (CDS) [data set], https://doi.org/10.24381/cds.adbb2d47 (last access: 22 October 2025), 2023b.

Hersbach, H., Bell, B., Berrisford, P., Hirahara, S., Horányi, A., Muñoz-Sabater, J., Nicolas, J., Peubey, C., Radu, R., Schepers, D., Simmons, A., Soci, C., Abdalla, S., Abellan, X., Balsamo, G., Bechtold, P., Biavati, G., Bidlot, J., Bonavita, M., De Chiara, G., Dahlgren, P., Dee, D., Diamantakis, M., Dragani, R., Flemming, J., Forbes, R., Fuentes, M., Geer, A., Haimberger, L., Healy, S., J. Hogan, R., Hólm, E., Janisková, M., Keeley, S., Laloyaux, P., Lopez, P., Lupu, C., Radnoti, G., de Rosnay, P., Rozum, I., Vamborg, F., Villaume, S., Thépaut, J.-N.: The ERA5 global reanalysis, Q. J. Roy. Meteor. Soc., 146, 1999-2049, https://doi.org/10.1002/qj.3803, 2020.

Hilton, T. W., Davis, K. J., Keller, K., and Urban, N. M.: Improving North American terrestrial CO_2 flux diagnosis using spatial structure in land surface model residuals, Biogeosciences, 10, 4607–4625, https://doi.org/10.5194/bg-10-4607-2013, 2013.

Hong, J. and Kim, J.: Impact of the Asian monsoon climate on ecosystem carbon and water exchanges: a wavelet analysis and its ecosystem modeling implications, Global Change Biology, 17, 1900–1916, https://doi.org/10.1111/j.1365-2486.2010.02337.x, 2011.

Hong, J.-W., Hong, J., Chun, J., Lee, Y. H., Chang, L.-S., Lee, J.-B., Yi, K., Park, Y.-S., Byun, Y.-H., and Joo, S.: Comparative assessment of net CO_2 exchange across an urbanization gradient in Korea based on eddy covariance measurements, Carbon Balance and Management, 14, 13, https://doi.org/10.1186/s13021-019-0128-6, 2019.

Hong, J.-W., Lee, S.-D., Lee, K., and Hong, J.: Seasonal variations in the surface energy and CO_2 flux over a high-rise, high-population, residential urban area in the East Asian monsoon region, International Journal of Climatology, 40, 4384–4407, https://doi.org/10.1002/joc.6463, 2020.

Hsu, C.-H., Henze, D. K., Mizzi, A. P., Abad, G. G., He, J., Harkins, C., Naeger, A. R., Lyu, C., Liu, X., Miller, C. C., Pierce, R. B., Johnson, M. S., and McDonald, B. C.: An Observing System Simulation Experiment Analysis of How Well Geostationary Satellite Trace-Gas Observations Constrain NOx Emissions in the US, Journal of Geophysical Research: Atmospheres, 129, e2023JD039323, https://doi.org/10.1029/2023JD039323, 2024.

Huang, Y., Wei, J., Jin, J., Zhou, Z., and Gu, Q.: CO Fluxes in Western Europe during 2017–2020 Winter Seasons Inverted by WRF-Chem/Data Assimilation Research Testbed with MOPITT Observations, Remote Sensing, 14, 1133, https://doi.org/10.3390/rs14051133, 2022.

Hutchins, M. G., Colby, J. D., Marland, G., and Marland, E.: A comparison of five high-resolution spatially-explicit, fossil-fuel, carbon dioxide emission inventories for the United States, Mitig Adapt Strateg Glob Change, 22, 947–972, https://doi.org/10.1007/s11027-016-9709-9, 2017.

Inness, A., Ades, M., Agustí-Panareda, A., Barré, J., Benedictow, A., Blechschmidt, A.-M., Dominguez, J. J., Engelen, R., Eskes, H., Flemming, J., Huijnen, V., Jones, L., Kipling, Z., Massart, S., Parrington, M., Peuch, V.-H., Razinger, M., Remy, S., Schulz, M., and Suttie, M.: The CAMS reanalysis of atmospheric composition, Atmospheric Chemistry and Physics, 19, 3515–3556, https://doi.org/10.5194/acp-19-3515-2019, 2019.

IPCC: Climate Change 2021: The Physical Science Basis. Contribution of Working Group I to the Sixth Assessment Report of the Intergovernmental Panel on Climate Change, edited by: Masson-Delmotte, V., Zhai, P., Pirani, A., Connors, S. L., Péan, C., Berger, S., Caud, N., Chen, Y., Goldfarb, L., Gomis, M. I., Huang, M., Leitzell, K., Lonnoy, E., Matthews, J. B. R., Maycock, T. K., Waterfield, T., Yelekçi, O., Yu, R., and Zhou, B., Cambridge University Press, https://doi.org/10.1017/9781009157896, 2021.

Janssens-Maenhout, G., Crippa, M., Guizzardi, D., Muntean, M., Schaaf, E., Dentener, F., Bergamaschi, P., Pagliari, V., Olivier, J. G. J., Peters, J. A. H. W., van Aardenne, J. A., Monni, S., Doering, U., Petrescu, A. M. R., Solazzo, E., and Oreggioni, G. D.: EDGAR v4.3.2 Global Atlas of the three major greenhouse gas emissions for the period 1970–2012, Earth System Science Data, 11, 959–1002, https://doi.org/10.5194/essd-11-959-2019, 2019.

Janssens-Maenhout, G., Pinty, B., Dowell, M., Zunker, H., Andersson, E., Balsamo, G., Bézy, J.-L., Brunhes, T., Bösch, H., Bojkov, B., Brunner, D., Buchwitz, M., Crisp, D., Ciais, P., Counet, P., Dee, D., Denier Van Der Gon, H., Dolman, H., Drinkwater, M. R., Dubovik, O., Engelen, R., Fehr, T., Fernandez, V., Heimann, M., Holmlund, K., Houweling, S., Husband, R., Juvyns, O., Kentarchos, A., Landgraf, J., Lang, R., Löscher, A., Marshall, J., Meijer, Y., Nakajima, M., Palmer, P. I., Peylin, P., Rayner, P., Scholze, M., Sierk, B., Tamminen, J., and Veefkind, P.: Toward an Operational Anthropogenic CO_2 Emissions Monitoring and Verification Support Capacity, Bulletin of the American Meteorological Society, 101, E1439–E1451, https://doi.org/10.1175/BAMS-D-19-0017.1, 2020.

Jiménez, P. A., Dudhia, J., González-Rouco, J. F., Navarro, J., Montávez, J. P., and García-Bustamante, E.: A Revised Scheme for the WRF Surface Layer Formulation, Monthly Weather Review, 140, 898–918, https://doi.org/10.1175/MWR-D-11-00056.1, 2012.

Jin, J., Huang, Y., Wei, C., Wang, X., Xu, X., Gu, Q., and Wang, M.: Analysis of CO_2 Concentration and Fluxes of Lisbon Portugal Using Regional CO_2 Assimilation Method Based on WRF-Chem, Atmosphere, 16, https://doi.org/10.3390/atmos16070847, 2025.

Jo, Y. H., Kim, S. H., Lee, Y. G., Kim, C. K., Hong, J., Lee, J., and Jang, K.: Evaluation of Topographic Effect Parameterizations in Weather Research and Forecasting Model over Complex Mountainous Terrain in Wildfire-Prone Regions, Fire, 8, https://doi.org/10.3390/fire8050196, 2025.

Jung, M., Henkel, K., Herold, M., and Churkina, G.: Exploiting synergies of global land cover products for carbon cycle modeling, Remote Sensing of Environment, 101, 534–553, https://doi.org/10.1016/j.rse.2006.01.020, 2006.

Kang, J.-S., Kalnay, E., Liu, J., Fung, I., Miyoshi, T., and Ide, K.: "Variable localization" in an ensemble Kalman filter: Application to the carbon cycle data assimilation, Journal of Geophysical Research: Atmospheres, 116, https://doi.org/10.1029/2010JD014673, 2011.

Kang, J.-S., Kalnay, E., Miyoshi, T., Liu, J., and Fung, I.: Estimation of surface carbon fluxes with an advanced data assimilation methodology, Journal of Geophysical Research: Atmospheres, 117, https://doi.org/10.1029/2012JD018259, 2012.

Kim, J., Shin, H.-J., Lee, K., and Hong, J.: Enhancement of ANN-based wind power forecasting by modification of surface roughness parameterization over complex terrain, Journal of Environmental Management, 362, 121246, https://doi.org/10.1016/j.jenvman.2024.121246, 2024.

Kwon, D., Hong, J., and Koo, B.: WRF-Chem/DART inversion system for CO_2 and CH_4 emissions in Korea, Zenodo [data set], https://doi.org/10.5281/zenodo.16939122 (last access: 15 October 2025), 2025a

Kwon, D., Hong, J., and Koo, B.: WRF-Chem/DART inversion dataset for CO_2 and CH_4 emissions in Korea, Zenodo [data set], https://doi.org/10.5281/zenodo.16947463 (last access: 15 October 2025), 2025b

Kwon, D., Hong, J., and Koo, B.: Data for: Regional CO2 and CH4 inversion system using WRF-Chem (v4.4)/DART (v9.8.0) and continuous high-precision observations over the Korean Peninsula, Zenodo [data set], https://doi.org/10.5281/zenodo.17402804 (last access: 24 October 2025), 2025c

Lauvaux, T., Miles, N. L., Deng, A., Richardson, S. J., Cambaliza, M. O., Davis, K. J., Gaudet, B., Gurney, K. R., Huang, J., O'Keefe, D., Song, Y., Karion, A., Oda, T., Patarasuk, R., Razlivanov, I., Sarmiento, D., Shepson, P., Sweeney, C., Turnbull, J., and Wu, K.: High-resolution atmospheric inversion of urban CO2 emissions during the dormant season of the Indianapolis Flux Experiment (INFLUX), Journal of Geophysical Research: Atmospheres, 121, 5213–5236, https://doi.org/10.1002/2015JD024473, 2016.

Lauvaux, T., Gurney, K. R., Miles, N. L., Davis, K. J., Richardson, S. J., Deng, A., Nathan, B. J., Oda, T., Wang, J. A., Hutyra, L., and Turnbull, J.: Policy-Relevant Assessment of Urban CO2 Emissions, Environ. Sci. Technol., 54, 10237–10245, https://doi.org/10.1021/acs.est.0c00343, 2020.

Lee, H., Han, S.-O., Ryoo, S.-B., Lee, J.-S., and Lee, G.-W.: The measurement of atmospheric CO2 at KMA GAW regional stations, its characteristics, and comparisons with other East Asian sites, Atmospheric Chemistry and Physics, 19, 2149–2163, https://doi.org/10.5194/acp-19-2149-2019, 2019.

Lee, H., Seo, W., Li, S., Lee, S., Kenea, S. T., and Joo, S.: Measurement report: Atmospheric CH_4 at regional stations of the Korea Meteorological Administration–Global Atmosphere Watch Programme: measurement, characteristics, and long-term changes of its drivers, Atmos. Chem. Phys., 23, 7141–7159, https://doi.org/10.5194/acp-23-7141-2023, 2023.

Lee, J. and Hong, J.: Implementation of spaceborne lidar-retrieved canopy height in the WRF model, Journal of Geophysical Research: Atmospheres, 121, 6863–6876, https://doi.org/10.1002/2015JD024299, 2016.

Lee, J., Hong, J., Noh, Y., and Jiménez, P. A.: Implementation of a roughness sublayer parameterization in the Weather Research and Forecasting model (WRF version 3.7.1) and its evaluation for regional climate simulations, Geoscientific Model Development, 13, 521–536, https://doi.org/10.5194/gmd-13-521-2020, 2020.

Lee, J., Shin, H. H., Hong, S.-Y., Jiménez, P. A., Dudhia, J., and Hong, J.: Impacts of subgrid-scale orography parameterization on simulated surface layer wind and monsoonal precipitation in the high-resolution WRF model, Journal of Geophysical Research: Atmospheres, 120, 644–653, https://doi.org/10.1002/2014JD022747, 2015.

Lee, J.-H., Woo, H. J., Son, S.-K., Kim, M., Lee, D.-H., Tsunogai, U., and Jeong, K.-S.: Flux and distribution of methane (CH4) in the Gunsan Basin of the southeastern Yellow Sea, off the Western Korea, Journal of Environmental Science and Health, Part A, 53, 457–466, https://doi.org/10.1080/10934529.2017.1409026, 2018.

Lee, K., Hong, J.-W., Kim, J., and Hong, J.: Partitioning of net CO_2 exchanges at the city-atmosphere interface into biotic and abiotic components, MethodsX, 8, 101231, https://doi.org/10.1016/j.mex.2021.101231, 2021.

Li, X., Hu, X.-M., Cai, C., Jia, Q., Zhang, Y., Liu, J., Xue, M., Xu, J., Wen, R., and Crowell, S. M. R.: Terrestrial CO_2 Fluxes, Concentrations, Sources and Budget in Northeast China: Observational and Modeling Studies, Journal of Geophysical Research: Atmospheres, 125, e2019JD031686, https://doi.org/10.1029/2019JD031686, 2020.

Lim, K.-S. S., Lim, J.-M., Shin, H. H., Hong, J., Ji, Y.-Y., and Lee, W.: Impacts of subgrid-scale orography parameterization on simulated atmospheric fields over Korea using a high-resolution atmospheric forecast model, Meteorol Atmos Phys, 131, 975–985, https://doi.org/10.1007/s00703-018-0615-4, 2019.

Liu, X., Mizzi, A. P., Anderson, J. L., Fung, I., and Cohen, R. C.: Assimilation of satellite NO2 observations at high spatial resolution using OSSEs, Atmospheric Chemistry and Physics, 2017.

Locatelli, R., Bousquet, P., Chevallier, F., Fortems-Cheney, A., Szopa, S., Saunois, M., Agusti-Panareda, A., Bergmann, D., Bian, H., Cameron-Smith, P., Chipperfield, M. P., Gloor, E., Houweling, S., Kawa, S. R., Krol, M., Patra, P. K., Prinn, R. G., Rigby, M., Saito, R., and Wilson, C.: Impact of transport model errors on the global and regional methane emissions estimated by inverse modelling, Atmospheric Chemistry and Physics, 13, 9917–9937, https://doi.org/10.5194/acp-13-9917-2013, 2013.

Ma, C., Wang, T., Jiang, Z., Wu, H., Zhao, M., Zhuang, B., Li, S., Xie, M., Li, M., Liu, J., and Wu, R.: Importance of Bias Correction in Data Assimilation of Multiple Observations Over Eastern China Using WRF-Chem/DART, Journal of Geophysical Research: Atmospheres, 125, e2019JD031465, https://doi.org/10.1029/2019JD031465, 2020.

Mahadevan, P., Wofsy, S. C., Matross, D. M., Xiao, X., Dunn, A. L., Lin, J. C., Gerbig, C., Munger, J. W., Chow, V. Y., and Gottlieb, E. W.: A satellite-based biosphere parameterization for net ecosystem CO_2 exchange: Vegetation Photosynthesis and Respiration Model (VPRM), Global Biogeochemical Cycles, 22, https://doi.org/10.1029/2006GB002735, 2008.

Ministry of Environment, Republic of Korea: The Republic of Korea's First Biennial Transparency Report and Fifth National Communication under the UNFCCC and the Paris Agreement, available at: https://unfccc.int/documents/645637 (last access: 06 June 2025), 2025.

Mizzi, A. P., Arellano Jr., A. F., Edwards, D. P., Anderson, J. L., and Pfister, G. G.: Assimilating compact phase space retrievals of atmospheric composition with WRF-Chem/DART: a regional chemical transport/ensemble Kalman filter data assimilation system, Geoscientific Model Development, 9, 965–978, https://doi.org/10.5194/gmd-9-965-2016, 2016.

Mizzi, A. P., Edwards, D. P., and Anderson, J. L.: Assimilating compact phase space retrievals (CPSRs): comparison with independent observations (MOZAIC in situ and IASI retrievals) and extension to assimilation of truncated retrieval profiles, Geoscientific Model Development, 11, 3727–3745, https://doi.org/10.5194/gmd-11-3727-2018, 2018.

Moon, J., Shim, C., Seo, J., and Han, J.: Evaluation of Korean methane emission sources with satellite retrievals by spatial correlation analysis, Environ Monit Assess, 196, 296, https://doi.org/10.1007/s10661-024-12449-w, 2024.

Mueller, K. L., Lauvaux, T., Gurney, K. R., Roest, G., Ghosh, S., Gourdji, S. M., Karion, A., DeCola, P., and Whetstone, J.: An emerging GHG estimation approach can help cities achieve their climate and sustainability goals, Environ. Res. Lett., 16, 084003, https://doi.org/10.1088/1748-9326/ac0f25, 2021.

Nalini, K., Lauvaux, T., Abdallah, C., Lian, J., Ciais, P., Utard, H., Laurent, O., and Ramonet, M.: High-Resolution Lagrangian Inverse Modeling of CO_2 Emissions Over the Paris Region During the First 2020 Lockdown Period, Journal of Geophysical Research: Atmospheres, 127, e2021JD036032, https://doi.org/10.1029/2021JD036032, 2022.

National Centers for Environmental Prediction, National Weather Service, NOAA, and U.S. Department of Commerce: NCEP ADP Global Upper Air and Surface Weather Observations (PREPBUFR format), Research Data Archive at the National Center for Atmospheric Research, Computational and Information Systems Laboratory [data set], https://doi.org/10.5065/Z83F-N512 (last access: 22 October 2025), 2008.

Nisbet, E. G., Manning, M. R., Dlugokencky, E. J., Fisher, R. E., Lowry, D., Michel, S. E., Myhre, C. L., Platt, S. M., Allen, G., Bousquet, P., Brownlow, R., Cain, M., France, J. L., Hermansen, O., Hossaini, R., Jones, A. E., Levin, I., Manning, A. C., Myhre, G., Pyle, J. A., Vaughn, B. H., Warwick, N. J., and White, J. W. C.: Very Strong Atmospheric Methane Growth in the 4 Years 2014–2017: Implications for the Paris Agreement, Global Biogeochemical Cycles, 33, 318–342, https://doi.org/10.1029/2018GB006009, 2019.

Oda, T. and Maksyutov, S.: ODIAC Fossil Fuel CO_2 Emissions Dataset (Version name: ODIAC2022), Center for Global Environmental Research, National Institute for Environmental Studies [data set], https://doi.org/10.17595/20170411.001 (last access: 22 October 2025), 2015.

Oda, T., Maksyutov, S., and Andres, R. J.: The Open-source Data Inventory for Anthropogenic CO_2, version 2016 (ODIAC2016): a global monthly fossil fuel CO_2 gridded emissions data product for tracer transport simulations and surface flux inversions, Earth System Science Data, 10, 87–107, https://doi.org/10.5194/essd-10-87-2018, 2018.

Oda, T., Bun, R., Kinakh, V., Topylko, P., Halushchak, M., Marland, G., Lauvaux, T., Jonas, M., Maksyutov, S., Nahorski, Z., Lesiv, M., Danylo, O., and Horabik-Pyzel, J.: Errors and uncertainties in a gridded carbon dioxide emissions inventory, Mitig Adapt Strateg Glob Change, 24, 1007–1050, https://doi.org/10.1007/s11027-019-09877-2, 2019.

Ogle, S. M., Buendia, L., Butterbach-Bahl, K., Breidt, F. J., Hartman, M., Yagi, K., Nayamuth, R., Spencer, S., Wirth, T., and Smith, P.: Advancing national greenhouse gas inventories for agriculture in developing countries: improving activity data, emission factors and software technology, Environ. Res. Lett., 8, 015030, https://doi.org/10.1088/1748-9326/8/1/015030, 2013.

Pauw, W. P., Klein, R. J. T., Mbeva, K., Dzebo, A., Cassanmagnago, D., and Rudloff, A.: Beyond headline mitigation numbers: we need more transparent and comparable NDCs to achieve the Paris Agreement on climate change, Climatic Change, 147, 23–29, https://doi.org/10.1007/s10584-017-2122-x, 2018.

Pisso, I., Patra, P., Takigawa, M., Machida, T., Matsueda, H., and Sawa, Y.: Assessing Lagrangian inverse modelling of urban anthropogenic CO_2 fluxes using in situ aircraft and ground-based measurements in the Tokyo area, Carbon Balance and Management, 14, 6, https://doi.org/10.1186/s13021-019-0118-8, 2019.

Pouyaei, A., Mizzi, A. P., Choi, Y., Mousavinezhad, S., and Khorshidian, N.: Downwind Ozone Changes of the 2019 Williams Flats Wildfire: Insights From WRF-Chem/DART Assimilation of OMI NO2, HCHO, and MODIS AOD Retrievals, Journal of Geophysical Research: Atmospheres, 128, e2022JD038019, https://doi.org/10.1029/2022JD038019, 2023.

Rayner, P. J., Raupach, M. R., Paget, M., Peylin, P., and Koffi, E.: A new global gridded data set of CO_2 emissions from fossil fuel combustion: Methodology and evaluation, Journal of Geophysical Research: Atmospheres, 115, https://doi.org/10.1029/2009JD013439, 2010.

Rogelj, J., Den Elzen, M., Höhne, N., Fransen, T., Fekete, H., Winkler, H., Schaeffer, R., Sha, F., Riahi, K., and Meinshausen, M.: Paris Agreement climate proposals need a boost to keep warming well below 2 °C, Nature, 534, 631–639, https://doi.org/10.1038/nature18307, 2016.

Roobaert, A., Laruelle, G. G., Landschützer, P., and Regnier, P.: Uncertainty in the global oceanic CO_2 uptake induced by wind forcing: quantification and spatial analysis, Biogeosciences, 15, 1701–1720, https://doi.org/10.5194/bg-15-1701-2018, 2018.

Roobaert, A., Laruelle, G. G., Landschützer, P., Gruber, N., Chou, L., and Regnier, P.: The Spatiotemporal Dynamics of the Sources and Sinks of CO_2 in the Global Coastal Ocean, Global Biogeochemical Cycles, 33, 1693–1714, https://doi.org/10.1029/2019GB006239, 2019.

Schroeder, W., Oliva, P., Giglio, L., and Csiszar, I. A.: The New VIIRS 375 m active fire detection data product: Algorithm description and initial assessment, Remote Sensing of Environment, 143, 85–96, https://doi.org/10.1016/j.rse.2013.12.008, 2014.

Segato, D., Graziosi, F., and Manca, G.: Evaluation of Copernicus atmosphere monitoring service methane products 2019-2023, Publications Office of the European Union, https://data.europa.eu/doi/10.2760/8653047, 2025.

Shim, C., Han, J., Henze, D. K., and Yoon, T.: Identifying local anthropogenic CO_2 emissions with satellite retrievals: a case study in South Korea, International Journal of Remote Sensing, 40, 1011–1029, https://doi.org/10.1080/01431161.2018.1523585, 2019.

Sijikumar, S., Raju, A., Valsala, V., Tiwari, Y., Girach, I. A., Jain, C. D., and Ratnam, M. V.: High-Resolution Bayesian Inversion of Carbon Dioxide Flux Over Peninsular India, Atmospheric Environment, 308, 119868, https://doi.org/10.1016/j.atmosenv.2023.119868, 2023.

Super, I., Denier van der Gon, H. A. C., van der Molen, M. K., Sterk, H. A. M., Hensen, A., and Peters, W.: A multi-model approach to monitor emissions of CO_2 and CO from an urban–industrial complex, Atmospheric Chemistry and Physics, 17, 13297–13316, https://doi.org/10.5194/acp-17-13297-2017, 2017.

UNFCCC: Adoption of the Paris Agreement. Report No. FCCC/CP/2015/L.9/ Rev.1, available at: https://unfccc.int/resource/docs/2015/cop21/eng/l09r01.pdf (last access: 22 October 2025), 2015.

van der Velde, I. R., Miller, J. B., van der Molen, M. K., Tans, P. P., Vaughn, B. H., White, J. W. C., Schaefer, K., and Peters, W.: The CarbonTracker Data Assimilation System for CO_2 and $\delta^{13}C$ (CTDAS-C13 v1.0): retrieving information on land–atmosphere exchange processes, Geoscientific Model Development, 11, 283–304, https://doi.org/10.5194/gmd-11-283-2018, 2018.

Velasco, E., Segovia, E., and Roth, M.: High-resolution maps of carbon dioxide and moisture fluxes over an urban neighborhood, Environ. Sci.: Atmos., 3, 1110–1123, https://doi.org/10.1039/D2EA00108J, 2023.

Wang, Y., Yuan, Q., Li, T., Yang, Y., Zhou, S., and Zhang, L.: Seamless mapping of long-term (2010-2020) daily global XCO_2 and XCH_4 from the Greenhouse Gases Observing Satellite (GOSAT), Orbiting Carbon Observatory 2 (OCO-2), and CAMS global greenhouse gas reanalysis (CAMS-EGG4) with a spatiotemporally self-supervised fusion method, Earth System Science Data, 15, 3597-3622, https://doi.org/10.5194/essd-15-3597-2023, 2023.

Weber, T., Wiseman, N. A., and Kock, A.: Global ocean methane emissions dominated by shallow coastal waters, Nat Commun, 10, 4584, https://doi.org/10.1038/s41467-019-12541-7, 2019.

Weiss, R. F. and Prinn, R. G.: Quantifying greenhouse-gas emissions from atmospheric measurements: a critical reality check for climate legislation, Philosophical Transactions of the Royal Society A: Mathematical, Physical and Engineering Sciences, 369, 1925–1942, https://doi.org/10.1098/rsta.2011.0006, 2011.

Wiedinmyer, C. and Emmons, L.: Fire Inventory from NCAR version 2 Fire Emission. Research Data Archive at the National Center for Atmospheric Research, Computational and Information Systems Laboratory [data set], https://doi.org/10.5065/XNPA-AF09 (last access: 22 October 2025), 2022.

Wiedinmyer, C., Akagi, S. K., Yokelson, R. J., Emmons, L. K., Al-Saadi, J. A., Orlando, J. J., and Soja, A. J.: The Fire INventory from NCAR (FINN): a high resolution global model to estimate the emissions from open burning, Geoscientific Model Development, 4, 625–641, https://doi.org/10.5194/gmd-4-625-2011, 2011.

Wiedinmyer, C., Kimura, Y., McDonald-Buller, E. C., Emmons, L. K., Buchholz, R. R., Tang, W., Seto, K., Joseph, M. B., Barsanti, K. C., Carlton, A. G., and Yokelson, R.: The Fire Inventory from NCAR version 2.5: an updated global fire emissions model for climate and chemistry applications, Geoscientific Model Development, 16, 3873–3891, https://doi.org/10.5194/gmd-16-3873-2023, 2023.

WMO: IG3IS Urban Greenhouse Gas Emission Observation and Monitoring Good Research Practice Guidelines, WMO GAW Report No 275, available at: https://library.wmo.int/idurl/4/58055, 2022.

WMO: Integrated Global Greenhouse Gas Information System Good Practice Guidance for Estimating National-scale Greenhouse Gas Emissions using Atmospheric Observations, WMO GAW Report No. 319, available at: https://library.wmo.int/idurl/4/69714, 2025.

Zhang, Q., Li, M., Wang, M., Mizzi, A. P., Huang, Y., Wei, C., Jin, J., and Gu, Q.: CO_2 Flux over the Contiguous United States in 2016 Inverted by WRF-Chem/DART from OCO-2 XCO2 Retrievals, Remote Sensing, 13, 2996, https://doi.org/10.3390/rs13152996, 2021a.

Zhang, Q., Li, M., Wei, C., Mizzi, A. P., Huang, Y., and Gu, Q.: Assimilation of OCO-2 retrievals with WRF-Chem/DART: A case study for the Midwestern United States, Atmospheric Environment, 246, 118106, https://doi.org/10.1016/j.atmosenv.2020.118106, 2021b.

Zhang, Z., Poulter, B., Melton, J. R., Riley, W. J., Allen, G. H., Beerling, D. J., Bousquet, P., Canadell, J. G., Fluet-Chouinard, E., Ciais, P., Gedney, N., Hopcroft, P. O., Ito, A., Jackson, R. B., Jain, A. K., Jensen, K., Joos, F., Kleinen, T., Knox, S. H., Li, T., Li, X., Liu, X., McDonald, K., McNicol, G., Miller, P. A., Müller, J., Patra, P. K., Peng, C., Peng, S., Qin, Z., Riggs, R. M., Saunois, M., Sun, Q., Tian, H., Xu, X., Yao, Y., Xi, Y., Zhang, W., Zhu, Q., Zhu, Q., and Zhuang, Q.: Ensemble estimates of global wetland methane emissions over 2000–2020, Biogeosciences, 22, 305–321, https://doi.org/10.5194/bg-22-305-2025, 2025.

Zhao, X., Chen, J., Marshall, J., Gałkowski, M., Hachinger, S., Dietrich, F., Shekhar, A., Gensheimer, J., Wenzel, A., and Gerbig, C.: Understanding greenhouse gas (GHG) column concentrations in Munich using the Weather Research and Forecasting (WRF) model, Atmospheric Chemistry and Physics, 23, 14325–14347, https://doi.org/10.5194/acp-23-14325-2023, 2023.

Zhao, Y., Saunois, M., Bousquet, P., Lin, X., Berchet, A., Hegglin, M. I., Canadell, J. G., Jackson, R. B., Dlugokencky, E. J., Langenfelds, R. L., Ramonet, M., Worthy, D., and Zheng, B.: Influences of hydroxyl radicals (OH) on top-down estimates of the global and regional methane budgets, Atmospheric Chemistry and Physics, 20, 9525–9546, https://doi.org/10.5194/acp-20-9525-2020, 2020.